Review

A Review of Global Navigation Satellite System (GNSS)-Based Dynamic Monitoring Technologies for Structural Health Monitoring

Nan Shen [1], **Liang Chen** [1,2,*], **Jingbin Liu** [1,2], **Lei Wang** [1,2], **Tingye Tao** [3], **Dewen Wu** [1] **and Ruizhi Chen** [1,2]

[1] State Key Laboratory of Information Engineering in Surveying, Mapping and Remote Sensing, Wuhan University, Wuhan 430079, China; nanshen@whu.edu.cn (N.S.); jingbin.liu@whu.edu.cn (J.L.); lei.wang@whu.edu.cn (L.W.); wudewen@whu.edu.cn (D.W.); ruizhi.chen@whu.edu.cn (R.C.)
[2] Collaborative Innovation Center for Geospatial Technology, Wuhan 430079, China
[3] Hefei University of Technology, Hefei 230009, China; 2018106190020@whu.edu.cn
[*] Correspondence: l.chen@whu.edu.cn

check for updates

Abstract: In the past few decades, global navigation satellite system (GNSS) technology has been widely used in structural health monitoring (SHM), and the monitoring mode has evolved from long-term deformation monitoring to dynamic monitoring. This paper gives an overview of GNSS-based dynamic monitoring technologies for SHM. The review is classified into three parts, which include GNSS-based dynamic monitoring technologies for SHM, the improvement of GNSS-based dynamic monitoring technologies for SHM, as well as denoising and detrending algorithms. The significance and progress of Real-Time Kinematic (RTK), Precise Point Position (PPP), and direct displacement measurement techniques, as well as single-frequency technology for dynamic monitoring, are summarized, and the comparison of these technologies is given. The improvement of GNSS-based dynamic monitoring technologies for SHM is given from the perspective of multi-GNSS, a high-rate GNSS receiver, and the integration between the GNSS and accelerometer. In addition, the denoising and detrending algorithms for GNSS-based observations for SHM and corresponding applications are summarized. Challenges of low-cost and widely covered GNSS-based technologies for SHM are discussed, and problems are posed for future research.

Keywords: dynamic monitoring; GNSS; SHM; accelerometer; high-rate; denoising; detrending

1. Introduction

Buildings are one of the most active places for human activities, so the safety of buildings is closely related to people's lives and property. The quality of the building, or external factors such as overload, earthquakes, etc., have an impact on the structure of the building, which seriously threatens people's lives and property. Therefore, the monitoring of these structures is of great significance.

The process of implementing a damage identification strategy for aerospace, civil and mechanical engineering infrastructure is referred to as structural health monitoring (SHM) [1–3]. SHM is related to people's well-being, and it has been proposed for decades. In Moss et al. [4] and Mita et al. [5], SHM has been deeply explored, and the conditions that the SHM system needs to meet have been identified. Three of these conditions are listed here: structural monitoring of external influences, deformation structure monitoring due to long-term factors, and assessment of structural integrity after earthquakes. From the above, it can be concluded that the SHM system must meet the requirements of dynamic monitoring and long-term monitoring. In Brownjohn et al. [6], the motivation of SHM is comprehensively introduced, the problems faced in SHM applications are listed, and SHM is considered

to be a continuous system identification of structural model parameters using time-dependent data. The SHM data signal may come from vibration or from slow quasi-static changes, which requires monitoring techniques in the SHM with monitoring capabilities of long-term, slow-moving, and short-term vibration [6,7]. The development of SHM is limited by many factors, such as system reliability, data storage and data overload, environmental factors, observation noise, data mining, and information presentation.

Global navigation satellite system (GNSS)-based deformation monitoring technology meets both the long-term monitoring and short-term monitoring requirements of structures. Compared with traditional monitoring technology, GNSS-based deformation monitoring has the following advantages:

- No need for visibility between monitoring points.
- Real-time monitoring.
- Weather independence.
- High precision.
- Dynamic deformation monitoring.
- Long-term deformation monitoring.

Due to these advantages, this positioning technology has been widely applied to deformation monitoring, and its applications to SHM have been systematically summarized in many articles.

In Ogaja et al. [8], the progress of Global Positioning System (GPS) technology in structural monitoring between 1997 and 2006 was reviewed: from early low-frequency monitoring to subsequent high-frequency monitoring, from early trials to later production applications. The trend of the GPS receiver sampling rate from 10 Hz to 100 Hz during these 10 years was given. The complementary relationship between the GPS technology and accelerometer in structural monitoring was analyzed. At the same time, the frequency coverage of the accelerometer and GPS in SHM was given. GNSS-based monitoring technology has been widely applied to bridge structure monitoring, from initial testing to current production applications, and typical examples of successful applications in recent years were listed. Natural factors and increasing traffic flow increase the load on the bridge, which requires structural health monitoring after the bridge is completed. The structural response is an important parameter in bridge health monitoring which can be used to identify possible problems by comparing it with design criteria [9,10]. In Yi et al. [9], the GPS-based technologies related to bridge health monitoring were summarized, and some activities of GPS-based bridge health monitoring were introduced. The development of dynamic monitoring techniques for bridge displacement changes caused by wind, pedestrians, vehicles and temperature changes was presented. Cases of GPS and other sensor integration for bridge dynamic monitoring, such as GPS and accelerometer integration, as well as GPS and total station integration, were given. Problems of GPS-based bridge dynamic monitoring, such as poor satellite geometries, tropospheric and ionospheric delays, multipath effects and multi-rate sensor fusion strategies, etc., were studied. In addition, in Im et al. [11], the development history of GPS-based SHM and some typical application cases were given. GPS-based SHM evolved from a static to dynamic process, and various data processing strategies were developed during the application process. The improved scheme of single-frequency receiver positioning technique and multi-path mitigation techniques were given respectively. Several schemes for evaluating the accuracy of GPS-based dynamic monitoring, such as accelerometers, electric sine wave exciters and motion simulators, were proposed. Data fusion algorithms of GPS and other sensors, as well as the deep application of GPS-based in SHM, were investigated. The advantages of GPS over traditional sensors and the problems faced by GPS-based SHM applications were discussed.

However, most of the reviews mentioned above are based on milestone applications; there are few reviews based on the development of GNSS. Over the past decade, GNSS has undergone tremendous changes: the popularity of network real-time kinematic (RTK), more available GNSS constellations, such as GLONASS, Galileo, Beidou and regional augmentation systems, and more available signals [12]. According to the GNSS user technology report [13], the majority of current

receivers support multi-GNSS, except for the reserved legacy ones using single or dual GNSS (GPS/GPS+GLONASS) for applications with low-performance requirements, or where multi-GNSS is not available due to local regulations. As of April 7, 2019, the civil signals provided by each GNSS and satellites in orbit are detailed in Table 1. Although there are so many GNSS constellations now, various augmentation systems and other technologies are still necessary to address the concerns of most users regarding accuracy, availability, and integrity [12,14]. High-rate (1 Hz or higher) [15,16] GNSS receivers are available for SHM, and several new GNSS measurement methods have been proposed to measure displacement directly rather than through the change of position.

Table 1. Signal and orbit detail of different global navigation satellite system (GNSS) Constellations (April 7, 2019).

System	Satellites in Operation	Regime(s)	Orbital Height	Civil Signals
GPS	31	MEO	20,180 km	L1 C/A, L2C, L5, L1C
GLONASS	24	MEO	19,130 km	L1OF, L2OF, L3OC
Galileo	22	MEO	23,222 km	E1, E5a, E5b
Beidou	33	GEO IGSO MEO	GEO-35,786 km IGSO-35,786 km MEO-21,528 km	B1I, B2I, B3I, B1C, B2a

MEO: medium earth orbit, GEO: geosynchronous earth orbit, IGSO: inclined geosynchronous orbit.

In addition, GNSS positioning accuracy is affected by many factors, such as the atmosphere, multipath, and observation noise. Therefore, denoising and detrending techniques must be adopted to extract the information we are concerned about. What's more, the coverage of GNSS-based dynamic monitoring applications is expanding, and the requirements for a real-time, highly-reliable and low-cost system are more stringent.

Therefore, this paper aims at reviewing the GNSS-based dynamic monitoring technologies for SHM from the perspective of the development of GNSSs. In the following, Section 2 introduces GNSS-based dynamic monitoring technologies for SHM; Section 3 presents the technologies to improve GNSS-based dynamic monitoring for SHM; Section 4 details the denoising and detrending algorithms applied to GNSS measurement; finally, Section 5 summarizes the main points of the review, focusing on the progress of GNSS-based dynamic monitoring technologies.

2. GNSS-Based Dynamic Monitoring Technologies for Structural Health Monitoring (SHM)

In this paper, GNSS-based dynamic monitoring technologies are mainly classified into three categories: real-time kinematic (RTK), precise point position (PPP), and direct displacement measurements. RTK is widely applied to deformation monitoring and is the most mature technology compared to the other GNSS-based monitoring technologies. PPP technology has been a research hotspot in recent years. Direct displacement measurement is an innovative application of GNSS technology.

Pseudoranges and carrier phases are the basic GNSS observations used for positioning. The basic observation equations of pseudoranges and carrier phases are listed as follows [17]:

$$\left. \begin{aligned} R_i &= \rho + c\delta t_r - c\delta t^s - \delta I_{\Phi i} + \delta_{trop} + \delta M_R + \varepsilon_{Ri} \\ \Phi_i &= \rho + c\delta t_r - c\delta t^s + \delta I_{\Phi i} + \delta_{trop} - \lambda_i N_i + \delta M_\Phi + \varepsilon_{\Phi i} \end{aligned} \right\} \tag{1}$$

where i represents the ith frequency; λ_i is the wavelength of the carrier phase; R_i is the pseudorange observation; c is the speed of light in vacuum; δt_r is the receiver clock error; δt^s is the satellite clock error; Φ_i is the carrier-phase observation; ρ is the geometric distance between receiver and satellite; δ_{trop} is the tropospheric delay between receiver and satellite; $\delta I_{\Phi i}$ is the ionospheric delay between receiver and satellite; N_i is the integer ambiguity; δM_R is the pseudorange multipath error; δM_Φ is the carrier-phase

multipath error; ε_{Ri} is the pseudorange random measurement noise; $\varepsilon_{\Phi i}$ is the carrier-phase random measurement noise; The ionospheric error has the same absolute value but opposite sign on code- and carrier-phase measurements [18].

2.1. Real-Time Kinematic (RTK)

In RTK, the coordinates of the target point are determined by calculating the baseline vector between the target point and the reference point. Normally, the coordinate of the reference point is determined accurately by GNSS or other methods. Relative positioning requires simultaneous observation of the target and reference points [17]. The basic concept of relative positioning is demonstrated in Figure 1. A denotes the reference point, B denotes the unknown point, and b_{AB} denotes the baseline vector. The relationship between the three can be described as [17]:

$$X_B = X_A + b_{AB} \tag{2}$$

where X_B, X_A denote the position of point A and point B.
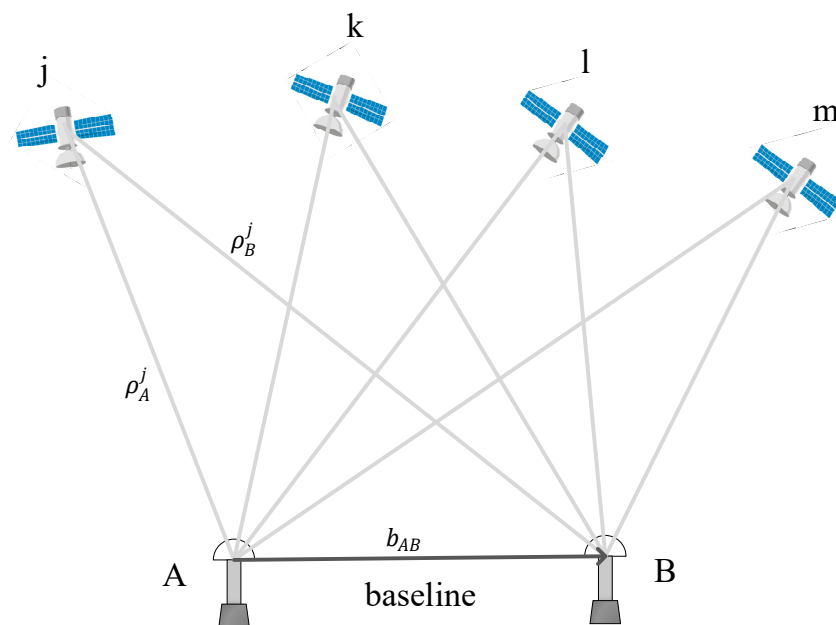
Figure 1. Basic concept of relative positioning [17].

Single difference observation and double difference observation are widely used as combined observations to eliminate satellite clock error, receiver clock error, integer ambiguity, and other parameters. The single difference observation for satellite j across receiver A and B in Figure 1 can be derived from the basic observation as [19]:

$$\left. \begin{aligned} \nabla R_{i\,AB}^{j} &= R_{i\,B}^{j} - R_{i\,A}^{j} \\ \nabla \Phi_{i\,AB}^{j} &= \Phi_{i\,B}^{j} - \Phi_{i\,A}^{j} \end{aligned} \right\} \tag{3}$$

The following single difference observation can be obtained by substituting the formula 1 into formula 3.

$$\left. \begin{aligned} \nabla R_{i\,AB}^{j} &= \nabla \rho_{AB}{}^{j} + c\nabla \delta t_{r_{AB}} - \nabla \delta I_{\Phi iAB}{}^{j} + \nabla \delta_{tropAB}{}^{j} + \nabla \delta M_{RAB}{}^{j} + \nabla \varepsilon_{RiAB}{}^{j} \\ \nabla \Phi_{i\,AB}^{j} &= \nabla \rho_{AB}{}^{j} + c\nabla \delta t_{r_{AB}} + \nabla \delta I_{\Phi iAB}{}^{j} + \nabla \delta_{tropAB}{}^{j} - \lambda_i \nabla N_{iAB}{}^{j} + \nabla \delta M_{\Phi AB}{}^{j} + \nabla \varepsilon_{\Phi iAB}{}^{j} \end{aligned} \right\} \tag{4}$$

where ∇ denotes the single difference operator between receiver A and B; the satellite clock error item can be eliminated from the single difference observation.

The double difference observation equation of relative positioning among receivers A, B and satellites k, j can be derived from the single difference observation in the same way [19]:

$$\left.\begin{array}{l} \Delta\nabla\mathrm{R}_{i_{AB}}^{jk} = \Delta\nabla\rho_{AB}{}^{jk} - \Delta\nabla\delta I_{\Phi i AB}{}^{jk} + \Delta\nabla\delta_{trop AB}{}^{jk} + \Delta\nabla\delta M_{R AB}{}^{jk} + \Delta\nabla\varepsilon_{R i AB}{}^{jk} \\ \Delta\nabla\Phi_{i_{AB}}^{jk} = \Delta\nabla\rho_{AB}{}^{jk} + \Delta\nabla\delta I_{\Phi i AB}{}^{jk} + \Delta\nabla\delta_{trop AB}{}^{jk} - \lambda_i\Delta\nabla N_{i AB}{}^{jk} + \Delta\nabla\delta M_{\Phi AB}{}^{jk} + \Delta\nabla\varepsilon_{\Phi i AB}{}^{jk} \end{array}\right\} \quad (5)$$

where $\Delta\nabla$ denotes double difference operator; the double-differenced observation not only eliminates the satellite clock-bias item but also eliminates the receiver error item. Also, for double difference observation, the atmospheric effects in the equation can be mostly eliminated if it is a short-baseline case. In actual work, satellites with longer observation times and higher elevation angles are generally selected as the reference satellites, and then the single-difference observations of the remaining satellites are respectively subtracted from the single-difference observations of the reference satellites to form a double-differenced observation equation [17]. The double-differenced observation equation should be linearized for further processing.

After forming the observation model, the integer ambiguity resolution (AR) method should be conducted. Integer AR is the key to high-precision positioning. The LAMBDA (Least-squares Ambiguity Decorrelation Adjustment) [20] method is usually adopted to complete this procedure. The GNSS AR process is divided into four steps [21–24]:

i.　　A standard least-squares adjustment is performed regardless of the integer constraints on the ambiguities. The 'float' solution can be obtained.

ii.　　The float ambiguities are used to compute the corresponding integer ambiguities using the integer least-square method.

iii.　A test is performed to decide whether to accept the calculated integer ambiguities.

iv.　The so-called fixed solution can be achieved by correcting the float solution of all other parameters with the integer ambiguities.

2.1.1. Application

RTK has been the most widely used GNSS technology in SHM for more than two decades and is also the most mature GNSS technology in SHM applications. Typical application scenarios for RTK in SHM include bridge and super high-rise building monitoring. Figure 2 shows a typical deployment scenario for RTK in bridge dynamic monitoring.
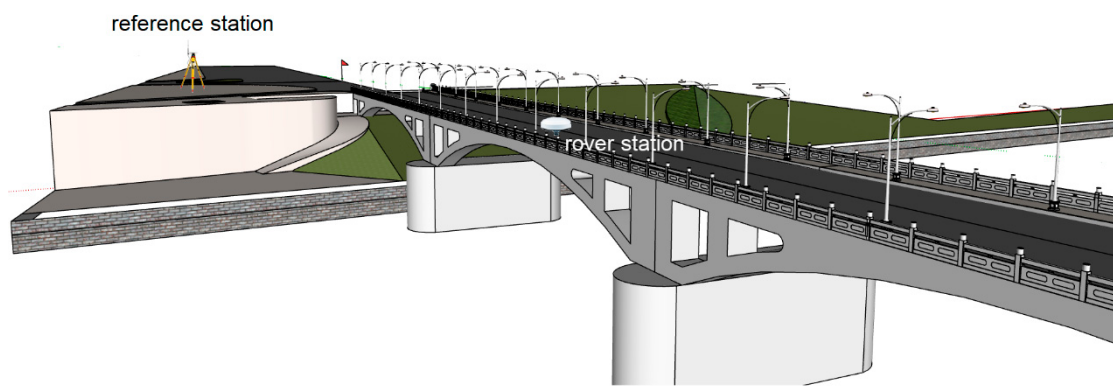

Figure 2. Typical deployment scenario for real-time kinematic (RTK) use in bridge dynamic monitoring.

For super-high building's dynamic monitoring, an RTK-based online structural monitoring system has been implemented for the 66th floor of the Republic Plaza Building in Singapore. The system is composed of three main subsystems [25]:

(1)　　A base station equipped with a geodetic GPS dual-frequency receiver was installed at a stable place nearby.

(2) Two dual-frequency receivers were installed on the 66th floor of the Republic Plaza Building as rover stations.

(3) A control center PC for running the monitoring software.

To aid local design code development, RTK was used to monitor super high-rise buildings to capture the dynamic response of buildings in the event of strong winds or distant earthquakes. The results were combined with accelerometer data to obtain the entire load frequency spectrum of the building.

For bridge dynamic monitoring, a series of experiments were conducted by the Surveying and Space Geodesy (IESSG) of the University of Nottingham to study GNSS-based technologies for bridge deformation monitoring [26–30]. An experiment was carried out on the suspended footbridge in Nottingham, which was measured by a combination of RTK and accelerometer. The sampling rates of GPS receivers and accelerometers are 10 Hz and 200 Hz, respectively. The reference station was installed on the shore near the bridge. An adaptive finite-duration impulse response (FIR) filter (AF) was employed to decompose the signal and noise. Spectral analysis and cross-correlation methods were used to analyze the characteristics of the multipath, as well as the relationship between the output of the adaptive filtering algorithm and input. The results demonstrate that this method can separate the multipath and random noise of the receiver from the real motion of the bridge [31]. Meng [32] conducted in-depth research on technologies using GPS-RTK and accelerometers for real-time deformation monitoring of bridges. Additionally, a series of experiments were conducted to verify the feasibility of the method and theory, including a controlled experiment on campus, experiments on the Suspension Footbridge in Nottingham Wilford, along with the London Millennium Bridge. The influence of the distribution of GPS satellites at that time on positioning accuracy was analyzed. There was a significant correlation between positioning accuracy and the geographic location of the receiver. In mid-latitude or high-latitude regions, the positioning accuracy of the north–south component is not as good as the positioning accuracy of the east–west component. To improve the positioning accuracy, signals from GLONASS were introduced. Pseudo-satellite technology was also proposed, and the simulation results show a significant improvement in GPS positioning accuracy. The AF method previously mentioned was introduced to mitigate noise [32–34] and will be detailed in Section 4.1.

2.1.2. The Limitations of RTK-Based Dynamic Monitoring

Over the past 20 years, RTK technology has been widely applied to SHM, and there are many successful applications, such as those mentioned above. However, from the perspective of the widespread application of SHM, cost, technical limitations, etc., the RTK technique still has many shortcomings:

- The reference station needs to be deployed at a stable place.
- When the reference station is also in the deformation zone, the method fails.
- The operation process is complicated and needs to be operated by professional surveying and mapping personnel.
- The reference and rover stations need to be observed at the same time, otherwise, no results will be obtained.
- The quality of the base station observation cannot be completely guaranteed, which will affect the positioning accuracy of the rover.
- The reference station receiver will increase monitoring costs.
- The rover's positioning accuracy depends on the distance to the reference station [35,36]

Traditional RTK technology cannot meet the requirements of large-scale production applications in traditional surveying and SHM. As an extension of RTK technology, network RTK technology can make up for the shortcomings of traditional RTK.

2.1.3. Network RTK

Network RTK is a high precision, real-time, carrier phase-based positioning technology.

The regional error correction model of network RTK is calculated using data from continuous operating reference stations (CORS) to provide position correction [35–39]. There are many ways to implement network RTK, of which the virtual reference station (VRS) is most commonly used. The purpose of the VRS technique is to convert the observation data obtained at the actual reference stations into observation data at the VRS position. The position of the user is then determined by the relative positioning between the VRS point and the user [17,40,41]. The VRS field set-up is shown in Figure 3. where A, B, C are reference stations; R is the rover station; V denotes the VRS. The observations of VRS can be obtained by the following formula [17]:

$$\Phi_r^s(X_V, t) = \Phi_r^s(X_A, t) + \frac{1}{\lambda^s}[\rho_r^s(X_V, t) - \rho_r^s(X_A, t)] + \Delta_r^s(X_V, t) \tag{6}$$

where r denotes receiver, s denotes satellite; $\Phi_r^s(X_V, t)$ is the VRS carrier phase observation for rover's relative positioning; X_V is the coordinate of VRS which can be set as the approximate coordinate of the user; $\Phi_r^s(X_A, t)$ is the carrier phase observation of reference station A; λ^s is the wavelength; $\rho_r^s(X_A, t)$ is the geometric distance from the reference station to the satellite; $\rho_r^s(X_V, t)$ is the geometric distance from the VRS to the satellite; $\Delta_r^s(X_V, t)$ contains orbital errors, ionospheric errors, tropospheric errors, etc., which can be estimated by the reference stations. Once the observation of the VRS is obtained, the user's position can be obtained by relative positioning. The main steps of implementing VRS are listed as follow [35].

(1) Data from the reference station network is transferred to the server for computing the models of orbital, ionospheric, tropospheric errors in $\Delta_r^s(X_V, t)$.

(2) The carrier phase ambiguities of the network baselines can be fixed and the actual error of network baselines can be calculated.

(3) The approximate position of the user receiver obtained by standard point positioning (SPP) with code measurements is usually adopted as the coordinate of the VRS X_V.

(4) The VRS coordinate X_V is transferred to the server, and linear or more sophisticated models are used to predict the errors $\Delta_r^s(X_V, t)$ at the VRS.

(5) The observation of VRS is generated by Equation (6) and transmitted to the user receiver in standard format.

(6) The relative positioning is adopted to calculate the position of user receiver.

Network RTK services are generally provided by service providers. Users generally obtain network RTK services in the form of leases. Compared with the traditional RTK, it has the following advantages:

- Users do not need to set up a reference station, the operation is simpler and faster.
- All users use a unified reference coordinate frame.
- Network RTK coverage is broader than that of traditional RTK [35].
- Network modeling for atmospheric correction.
- If the reference station is dense enough, the accuracy of the traditional RTK short baseline can be achieved.
- If there is a problem with one of the reference stations, the service can continue to be available. Network RTK has higher reliability and availability [42].
- Reduced user costs from a broad application perspective.
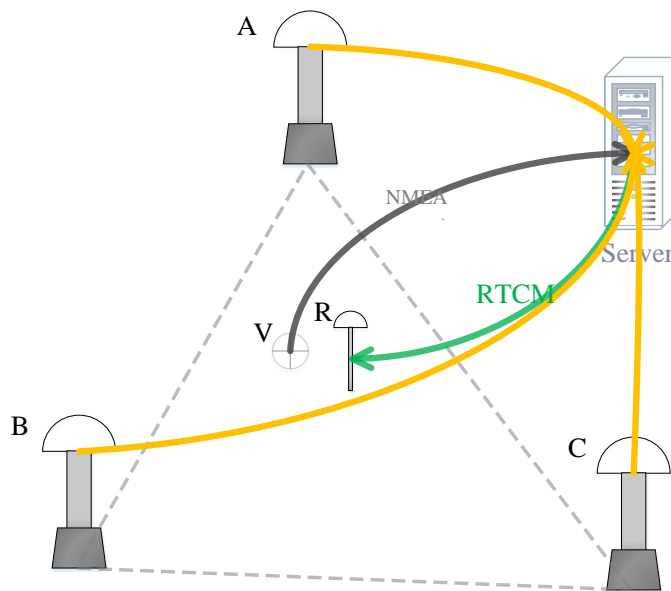
Figure 3. Virtual reference station (VRS) field set-up procedure [35,41].

RTK and postprocessing kinematic (PPK) technologies have long been used for monitoring of structures. However, network RTK has many advantages over traditional RTK, as mentioned above. Therefore, some scholars have tried to study network RTK for dynamic monitoring.

In Yu et al. [43], to verify the feasibility of network RTK in dynamic monitoring, laboratory and field experiments were designed and implemented respectively. The field test site was still the Welford Suspension Bridge in Nottingham, but the purpose was different from the previous one. Two GS10 receivers acted as rover stations, eliminating the effects of different receivers, and they received the same signal from a splitter connected to an antenna. Traditional RTK and Network RTK were adopted to position for the two receivers respectively. The differential corrections were provided by nearby reference station receiver and CORS service respectively. At the same time, the Kistler K-BEAM 8392A2 three-axis accelerometer data were collected for verification. The variation of the bridge was identified from the noisy network RTK result by the designed wavelet filtering scheme, and the vibration frequency was detected by Fourier transformation and wavelet spectrum analysis respectively. The findings demonstrate that Network RTK is a potential method for bridge dynamic monitoring. With hardware upgrades and algorithm optimization, it will be a useful tool for SHM [43,44].

Compared with traditional RTK, network RTK with wider coverage is more suitable for SHM. However, the current dynamic monitoring research based on network RTK is not detailed enough, and many problems remain to be studied, such as the impact of network density, the impact of monitoring location. Compared with the traditional RTK, network RTK is more flexible and can provide users with additional service for real-time ionospheric correction [42]. Table 2 summarizes the applications using RTK for dynamic monitoring. The information of experimental scene, aim, and measurement method are presented.

Table 2. Applications based on RTK for structural health monitoring (SHM).

Aim	Experimental Scene	Measurement Method	Literature
Implementation of online structural monitoring using RTK-GPS	A mechanical shaker and the Republic Plaza Building of Singapore		Ogaja et al. [25]
Real-time monitoring of the Humber Bridge	Field monitoring data of the Humber Bridge	RTK-GPS	Ashkenazi et al. [26,27]
Deflection monitoring of bridges by high-rate GPS	Platform and bridge trials		Roberts et al. [29]
Monitoring the deflections of large bridges using kinematic GPS and triaxial accelerometers	Nottingham Suspension Footbridge Trials	RTK-GPS and Accelerometer	Roberts et al. [28]
Multipath mitigation for structural deflection monitoring		RTK-GPS	Dodson et al. [31]
Real-time bridge deflection and vibration monitoring using an integrated system		RTK-GPS/accelerometer/pseudolite	Meng et al. [33]
Measurement of the dynamic displacements and of the modal frequencies	A short-span pedestrian bridge	RTK-GPS and Accelerometer	Moschas et al. [45]
Assessment of the measurements of low and high sampling frequencies of real-time GPS for structural movement monitoring	Mansoura railway bridge in Mansoura City, Egypt and Yonghe long-span bridge in China		Kaloop et al. [46]
Dynamic performance analysis of the towers of a long-span Bridge	Yonghe long-span bridge in China	RTK-GPS	Kaloop et al. [47]
A steel highway bridge monitoring and movement identification	Talkha highway steel bridge in Mansoura city, Egypt		Elnabwy et al. [48]
To validate the feasibility of the network RTK for the measurement of bridge dynamic responses	Laboratory Experiments and full-scale experiments were conducted on the Wilford suspension	Network RTK	Yu et al. [43]

2.2. Precise Point Position (PPP)

With precision satellite orbit and clock information, PPP can be used to achieve centimeter-level high-precision positioning [49–53]. The ionosphere-free combination observation equations of PPP are demonstrated as follows [52]:

$$
\left.\begin{array}{l}
\ell_P = \dfrac{R_1 f_1^2}{f_1^2 - f_2^2} - \dfrac{R_2 f_2^2}{f_1^2 - f_2^2} = \rho + c\Delta\delta + \Delta^{Trop} \\[2ex]
\ell_\Phi = \dfrac{\lambda_1 \Phi_1 f_1^2}{f_1^2 - f_2^2} - \dfrac{\lambda_2 \Phi_2 f_2^2}{f_1^2 - f_2^2} = \rho + c\Delta\delta + \Delta^{Trop} + \dfrac{\lambda_1 N_1 f_1^2}{f_1^2 - f_2^2} - \dfrac{\lambda_2 N_2 f_2^2}{f_1^2 - f_2^2}
\end{array}\right\}
\tag{7}
$$

where ℓ_P is the ionosphere-free combination observation of pseudoranges; ℓ_Φ is the ionosphere-free combination observation of carrier phases; R_1 and R_2 are the pseudorange observations; Φ_1 and Φ_2 are the carrier-phase observations; f_1 and f_2 are the frequencies; λ_1 and λ_2 denote wavelengths; ρ is the geometric distance from the station to the satellite; c is the speed of light in vacuum; $\Delta\delta$ is the station receiver clock offset; Δ^{Trop} is the tropospheric delay; N_1 and N_2 are the integer ambiguities; ρ can be expressed as a function of satellite coordinate $\left(X^S, Y^S, Z^S\right)$ and receiver coordinate (x, y, z):

$$
\rho = \sqrt{\left(X^S - x\right)^2 + \left(Y^S - y\right)^2 + \left(Z^S - z\right)^2}
\tag{8}
$$

The same AR process as mentioned in the Section 2.1 is also required, although the observation model is different [22]. To improve the accuracy of PPP and optimize the calculation results of PPP, the model must be refined. The model's refined content contains satellite antenna offset, phase winding correction, solid tide correction, ocean loading, earth rotation parameters, etc. For details please refer to the related references [52,54,55].

PPP is an approach that performs precise position determination using a single receiver without a reference station [49]. Many studies on the application of PPP in dynamic displacement monitoring have been carried out. To validate the performance of PPP in dynamic displacement monitoring, the Inertial Measurement Unit (IMU) or RTK is usually adopted as the reference.

In Xu et al. [56], to study the accuracy of high-rate PPP for the measurement of seismic wave motions in a short period, inertial measurement unit (IMU) data was adopted as the reference for experiments. The experiments are designed by taking many factors into consideration, such as the high sample rate to cover the frequency of large strong motion, and choke ring antenna to mitigate the effect of the multipath. The experimental platform is shown in Figure 4. The GPS data from experiments is processed by the software package Positioning And Navigation Data Analyst (PANDA) developed by the GNSS Research Center, Wuhan University. To compare the PPP displacement with the displacement from the IMU, the acceleration is integrated twice to obtain the displacement waveform. The integration process is performed by the software provided by the instrument maker. The results show that within a certain confidence interval, an accuracy of 2–4 mm in the horizontal direction and a vertical accuracy of 1.5–2 cm can be achieved in a short time.
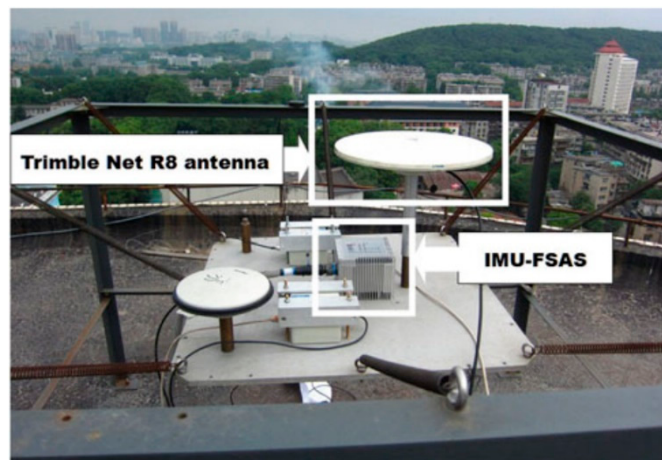

Figure 4. The experiment platform with the shake table, Trimble Net R8 [56].

In Yigit et al. [57], to assess the high-rate GNSS PPP method for detecting dynamic vertical displacement response of engineering structures, a series of oscillation tests were carried out. The experimental setup is as shown in Figure 5. The steel bar is fixed by the heavy concrete blocks and the rover receiver is fixed to the steel bar with the reference receiver set up nearby. Relative positioning between the reference and the rover receiver is adopted as the reference in this study. The three steel bars of different size are of different modal frequencies and can be calculated by taking into account the mass of the rover GNSS receiver. The GNSS data collected by the rover receiver on the bar is processed by an online PPP service named CSRS-PPP, developed by the Geodetic Survey Division of the NRCan (NRCan-GSD). The process is performed by using different GNSS orbit and clock products (EMU, rapid and IGS Final) in the kinematic mode. The displacement results show that the overall difference between PPP and relative positioning is within 10 mm and there is no obvious difference between PPP results using the IGS-Final and EMU ultra-rapid products in capturing dynamic oscillation.
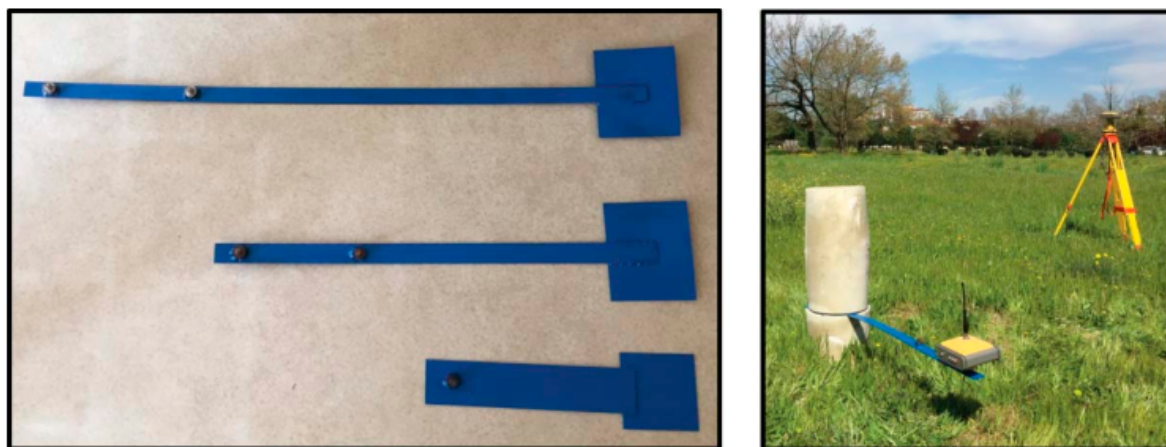
Figure 5. Steel bar models used in the study (left) and experimental set-up in the field [57].

At present, PPP-based dynamic monitoring for SHM is based on IGS precise ephemeris and clock products. The PPP-based dynamic monitoring for SHM based on real-time data stream service remains to be studied. Applications on dynamic monitoring using PPP are summarized as Table 3. The information of experimental scene, aim, and verification scheme are presented.

Table 3. Applications based on precise point position (PPP).

Aim	Experimental Scene	Verification Scheme	Literature
Mining deformation monitoring	IGS sites		Xu et al. [58] Hu et al. [59]
Measure seismic wave motions	GPS data and IMU data from shake table	IMU	Xu et al. [56]
Validation of performance of real-time kinematic PPP for deformation monitoring	Displacement monitoring test measured by telescopic pole		Martín et al. [60]
PPP sliding window algorithm for deformation monitoring	Simulation data and earthquake data		Song et al. [61]
Precise dynamic displacements detection	Field experiments	Different processing scenarios	Paziewski et al. [62]
High-rate PPP for detecting dynamic vertical displacement	ContT & RTK	Bar experiment	Yigit et al. [57,63]
PPP assessment of PPP accuracy for displacement waveforms	Acc & RTK	Experiment based on oscillator	Moschas et al. [64]
Epoch-wise station displacement	GPS seismology	Rapture model	Shi et al. [65]
Response analyses of Greece's earthquake based on GNSS-PPP	GPS seismology	Frequency domain analysis	Kaloop et al. [66]

Acc: Accelerometer, ContT: Controlled Test, IGS: International GNSS Service.

2.3. Displacement versus Position

The application of GPS in deformation monitoring is often used as a means of positioning to determine long-term or real-time deformation of structures. But for deformation, people are paying more attention to relative changes. Three methods for detecting displacement changes with direct displacement measurements are listed here.

2.3.1. Variometric Approach for Displacements Analysis Stand-Alone Engine (VADASE)

A method called Variometric Approach for Displacements Analysis Stand-Alone Engine (VADASE) was proposed to measure seismic waves [67]. The displacement variation is obtained by the difference between adjacent epochs of the high-frequency data. This method can be implemented by carrier

phase observation and broadcast ephemeris. Compared to traditional methods, reference station and precise ephemeris are not required in this method for monitoring real-time relative changes [67–73]. The core formula is as follows:

$$\alpha[\lambda\Delta\Phi_r^s]_{L1} + \beta[\lambda\Delta\Phi_r^s]_{L2} = (e_r^s \circ \Delta\xi_r + c\Delta\delta t_r) + \left([\Delta\rho_r^s]_{OR} - c\Delta\delta t^s + \Delta T_r^s\right) + \left([\Delta\rho_r^s]_{EtOl} + \Delta p_r^s\right) + \Delta m_r^s + \Delta\epsilon_r^s \tag{9}$$

where $\alpha = \left(f_{L1}^2/\left(f_{L1}^2 - f_{L2}^2\right)\right)$ and $\beta = \left(-f_{L2}^2/\left(f_{L1}^2 - f_{L2}^2\right)\right)$ are the coefficients of the ionosphere-free combination; Δ denotes the difference between consecutive epochs $(t, t+1)$; λ is the carrier phase wavelength; Φ_r^s is the carrier phase observation between the receiver and the satellite; $L_i(i = 1, 2)$ denotes the carrier phase; e_r^s is the unit vector from the satellite to the receiver; $\Delta\xi_r$ is the displacement between consecutive epochs; $\circ$ is the scalar product operator; c is the speed of light in vacuum; δt_r is the receiver clock error; $[\Delta\rho_r^s]_{OR}$ is the geometric range between the receiver and the satellite for the satellite's orbital motion and the Earth's rotation; δt^s is the satellite clock error; T_r^s is the tropospheric delay between the receiver and the satellite; $[\Delta\rho_r^s]_{EtOl}$ is the variation of the solid Earth tide and ocean loading; p_r^s is the sum of other effects; m_r^s is the multipath; ϵ_r^s is the noise; For detailed derivation process, please refer to the relevant reference [67].

There are four unknown parameters: $\Delta\xi_r$ and $\Delta\delta t_r$, and the other parameters can be compensated by models. To calculate the unknown parameters, at least four visible satellites are required in successive epochs. When the satellites number is greater than four, the least squares method is adopted to obtain the optimal solution. Assume that n satellites are viewed by the receiver both at epochs t and t + 1, the linearized observation modal of Equation (9) can be expressed as:

$$y = Ax + b + v \tag{10}$$

where $y[n \times 1]$ is the observation vector:

$$y_{n\times 1} = \begin{bmatrix} \alpha\left[\lambda\Delta\Phi_r^1\right]_{L1} + \beta\left[\lambda\Delta\Phi_r^1\right]_{L2} \\ \alpha\left[\lambda\Delta\Phi_r^2\right]_{L1} + \beta\left[\lambda\Delta\Phi_r^2\right]_{L2} \\ \vdots \\ \alpha\left[\lambda\Delta\Phi_r^i\right]_{L1} + \beta\left[\lambda\Delta\Phi_r^i\right]_{L2} \\ \vdots \\ \alpha[\lambda\Delta\Phi_r^n]_{L1} + \beta[\lambda\Delta\Phi_r^n]_{L2} \end{bmatrix} \tag{11}$$

$A[n \times 4]$ is the design matrix:

$$A_{n\times 4} = \begin{bmatrix} e_{rX}^1 & e_{rY}^1 & e_{rZ}^1 & 1 \\ e_{rX}^2 & e_{rY}^2 & e_{rZ}^2 & 1 \\ \vdots & \vdots & \vdots & \vdots \\ e_{rX}^i & e_{rY}^i & e_{rZ}^i & 1 \\ \vdots & \vdots & \vdots & \vdots \\ e_{rX}^n & e_{rY}^n & e_{rZ}^n & 1 \end{bmatrix} \tag{12}$$

$x[4 \times 1]$ is the unknown parameter vector:

$$x_{4\times 1} = \begin{bmatrix} \Delta\xi_r \\ \Delta\delta t_r \end{bmatrix} = \begin{bmatrix} \Delta X \\ \Delta Y \\ \Delta Z \\ \Delta\delta t_r \end{bmatrix} \tag{13}$$

$b[n \times 1]$ contains the known term:

$$b_{n\times 1} = \begin{bmatrix} \left[\Delta\rho_r^1\right]_{OR} - c\Delta\delta t^1 + \Delta T_r^1 \\ \left[\Delta\rho_r^2\right]_{OR} - c\Delta\delta t^2 + \Delta T_r^2 \\ \vdots \\ \left[\Delta\rho_r^i\right]_{OR} - c\Delta\delta t^i + \Delta T_r^i \\ \vdots \\ \left[\Delta\rho_r^n\right]_{OR} - c\Delta\delta t^n + \Delta T_r^n \end{bmatrix} \tag{14}$$

$v[n \times 1]$ is the noise of the observation; the weight matrix of the observation is decided by the cosine of the satellite zenith angle (Z_r^s):

$$W_{n\times n} = \begin{bmatrix} cos^2(Z_r^1) & 0 & \cdots & 0 \\ 0 & cos^2(Z_r^2) & \cdots & 0 \\ \vdots & \vdots & \ddots & \vdots \\ 0 & 0 & \cdots & cos^2(Z_r^n) \end{bmatrix} \tag{15}$$

The least square estimation of the unknown parameters can be achieved:

$$\hat{x} = \left(A^T W A\right)^{-1} A^T W (y - b) \tag{16}$$

When the displacement variation of each epoch is estimated, they can then can be regarded as the measured velocity, and the velocity can be integrated to obtain the displacement. Experiments have shown the potential of the VADASE method to detect displacement between adjacent epochs although the broadcast ephemeris is adopted, and the accuracy reaches the centimeter level. The main drawback of this method is the requirement for continuity between the data [67]. Many scholars have studied the applications of this method in seismology, and this method has been continuously improved.

Initially, simulation data were used to validate the algorithm. In Colosimo et al. [67], a carrier phase observation data stream that was shifted by Bernese software in actual GPS observations was used to test the method. The results calculated by this method are compared with the results calculated using the precision ephemeris. The results show that the horizontal and vertical velocity estimation accuracy of the method can reach 1–2 mm/s by using real-time GPS broadcast products. Next, the actual seismic GPS observation data are used to further verify the algorithm. In Colosimo et al. [67], Branzanti et al. [69], and Benedetti et al. [68], to verify the feasibility of this method in seismology, some actual seismic data was used to evaluate the method. The results show the potential of VADASE for real-time displacement and velocity, especially if implemented directly into the GPS receiver firmware. If this method can be implemented into the GPS receiver firmware, GPS would become a completely reliable system that supports monitoring slow deformation and vibration [67–69]. Furthermore, to verify the performance of the algorithm in single frequency case. In Benedetti et al. [68], to evaluate the accuracy that can be achieved with L1-only VADASE, and study the relationship between VADASE and sampling frequency, different sample rate data are processed by VADASE, the results are compared with the results from relative positioning and accelerometers. The results show that the accuracy of L1-only VADASE is slightly worse than the original VADASE, and the waveform reconstructed by this method becomes worse and worse as the sampling rate decreases, but the VADASE results are consistent with the L1-only VADASE results.

In addition, VADASE can also be applied to structural monitoring [74–76]. In Benedetti et al. [76], to exploit the performance of the low-cost GPS receiver uBlox 6 for small amplitude oscillatory motion monitoring, a one-direction vibrating table was used to assess the performance. The data was collected with vibration frequencies of 1.7 Hz, 2.0 Hz, 2.2 Hz, 2.7 Hz and amplitudes of 2 cm and 3 cm,

respectively. Due to the 5 Hz limit of the uBlox 6 sampling frequency, even in the lowest frequency test, there is an aliasing effect, resulting in an underestimation of about 30% of the oscillation amplitude and overall accuracy of about 30% of the reference solution [76]. In Ashcroft et al. [74], the VADASE-based automatic monitoring solution has been integrated into the GNSS receiver board for real-time dynamic monitoring of velocity and displacement without any time delay. The reference station type receiver Leica GR10/25 and the monitoring type Leica GM10 have this function. In the dynamic test, the velocity sensitivities in the east, north, and upper directions are 3.6 mm/s, 3.6 mm/s and 8 mm/s respectively; in the case of 1 Hz, the mean value of the dynamic displacement error in the east and north directions are 3.4 mm and 7.2 mm respectively; in the case of 10 Hz, the mean value of dynamic displacement error in the east and north directions are 5.8 mm and 3.5 mm, respectively.

The VADASE estimated displacement may be affected by two different factors: velocity false spikes due to outliers and trends in the displacement time series mainly due to broadcast orbit and clock errors [67,73]. In Fratarcangeli et al. [73], to solve these problems, a VADASE improvement solution called A-VADASE-LOO was proposed. This improved method has been applied to the seismic data actually collected recently. The processing results are compared with the post-processing PPP results and the Istituto Nazionale di Geofisica e Vulcanologia (INGV) static solution results. The results show that the consistency of A-VADASE-LOO and PPP in the horizontal component is better than 1 cm, and the vertical component is about 2 cm. The consistency of A-VADASE-LOO and INGV in the horizontal component is 0.5–1 cm, and the vertical component is 1–1.5 cm [73]. The VADASE method was born in GPS seismology and has been applied and developed in seismology.

Table 4 summarizes applications using VADASE for dynamic monitoring. The information of experimental scene, aim, method, application domain and verification scheme are presented.

Table 4. Applications based on the Variometric Approach for Displacements Analysis Stand-Alone Engine (VADASE) for SHM.

Aim	Experimental Scene	Application Domain	Method	Verification Scheme	Literature
Real-time GPS seismology with a stand-alone receiver	Simulation data and real earthquake data	GPS seismology	VADASE		Colosimo et al. [67]
Exploiting the VADASE algorithm	Earthquake data of GPS and accelerometer			Accelerometer	Benedetti et al. [68]
Near real-time, tsunami early warning system	Earthquake data from IGS sites			PPP and differential positioning	Branzanti et al. [69]
High-rate multi-GNSS observations for real-time capture of seismic waves	GPS and BDS data of an earthquake			Postprocessed GPS PPP and strong motion data	Geng et al. [71]
Performance evaluation of VADASE using very high-rate GPS	Moderate and large earthquakes			Postprocessed GPS PPP	Shu et al. [72]
GPS seismology for a moderate magnitude earthquake	High-rate GPS data of an earthquake		PPP, differential positioning, VADASE	Strong motion accelerometer	Hung et al. [70]
VADASE enhancement	GPS data of an earthquake		Improved VADASE	PPP	Fratarcangeli et al. [73]
VADASE onboard a stand-alone GNSS receiver	Static tests and controlled dynamic tests	Structural monitoring	VADASE		ASHCROFT et al. [74]
Different low-cost sensors for small amplitude oscillatory motion monitoring	One-direction vibrating table			High-speed, high-resolution camera	Benedetti et al. [76]

2.3.2. Phase Residual Method (PRM)

A single-frequency phase residual method (PRM) was proposed to detect vertical displacement [77]. The change detection of this method is also not based on the change of absolute position. It utilizes

double-difference phase observation; therefore, a reference station is required. The formula for calculating the double-difference phase is as follows [78]:

$$\lambda_i \Delta \nabla \phi_{i \text{AB}}^{jk}(t) = \Delta \nabla \rho_{AB}{}^{jk}(t) \quad -\lambda_i \Delta \nabla N_{iAB}{}^{jk} + \Delta \nabla \delta I_{\phi iAB}{}^{jk}(t) + +\Delta \nabla \delta_{trop AB}{}^{jk}(t)+ \\ \Delta \nabla \delta d_{\phi iAB}{}^{jk}(t) + \Delta \nabla \varepsilon_{\phi iAB}{}^{jk} \tag{17}$$

where t denotes time or epoch; $\Delta \nabla \delta d_{\phi iAB}{}^{jk}(t)$ is any other time dependent phase disturbance; Refer to Section 2.1 for the meaning of other symbols. The phase residual is derived as:

$$R(t) = \lambda_i \Delta \nabla \phi_{i \text{AB}}^{jk}(t) - trend(t) \tag{18}$$

where $R(t)$ is the phase residual; $trend(t)$ is the trending element which can be fitted to the polynomial function by previous double-difference phase observations.

To detect the oscillation in the vertical direction, there are certain requirements for the selection of the satellites: one satellite, called the measuring satellite, must be overhead and the other satellite, called the reference satellite, must be close to the horizon [77]. Satellites' space configuration in relation to the antenna is as Figure 6. In the Figure, DUM is the abbreviation of the device under measurement. With such configuration, the phase variation due to vertical displacement of the antenna will be minimal for the reference satellite but maximal for the measuring satellite. The antenna motion will not appear clearly in the raw residuals because of the components mentioned in Equation (6). To extract the antenna motion, eliminating all high-frequency noise caused by unexpected elements and reducing most of the low-frequency error caused by multipath, fast Fourier transformation (FFT) bandpass filter is adopted to clean up the data, leaving only the frequency describing the displacement [77].
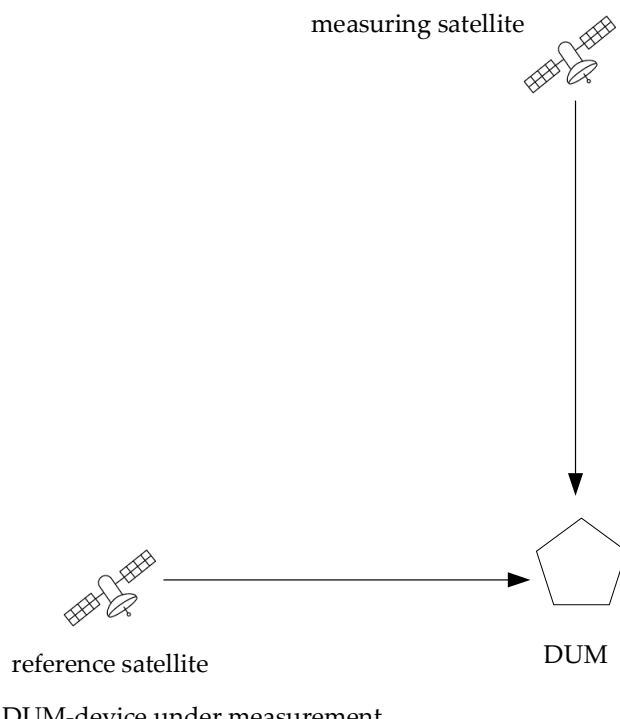

Figure 6. Satellites' space configuration in relation to the antenna [77].

Processing steps of PRM are summarized as follows:

- Select a pair of satellites as reference satellite and measurement satellite according to the criteria.
- Compute the double difference carrier phase observation by Equation (17).
- Compute the phase residual by Equation (18).

- Perform FFT band filtering to clean the phase residuals.

Please refer to the reference [77] for details.

To verify the feasibility of PRM for different sized bridges' dynamic monitoring, a number of experiments have been carried out. In Larocca et al. [79], the first application of the method was on a cable-stayed girder bridge built in 1967 in New Brunswick, Canada. Total station measurement data was used for verification in the experiment. The results show that the GPS data collected and processed by the PRM method well-matched the results obtained by total station measurement. This method has great potential for dynamic monitoring of medium-span bridges. In Larocca et al. [80], to verify that the GPS analyzed under PRM is available for dynamic monitoring of large structures, a test was conducted to monitor the Pierre-Laporte Suspension Bridge. A comparison was made between the improved GPS-OTF algorithm and the processing results obtained with PRM. Although the data and satellite selection strategies of the two algorithms are different, the calculated natural frequencies of the bridges are consistent. In Larocca et al. [81,82], to verify the feasibility of GPS monitoring for the structure of reinforced concrete road bridges, a series of experiments were carried out. This is also part of the continuous development of the previously proposed PRM method to increase the GPS detection threshold so that it could also be used for the dynamic monitoring of small reinforced concrete highway bridges. During the experimental period, the traffic remained open, and the data collected by GPS was processed by PRM, and continuous wavelet transformation was used for analysis. The finite element method (FEM) was applied to the bridge as a check. The results verify the consistency and feasibility of the dynamic performance for the concrete bridge monitored by this method [81,82]. So far, the PRM method has been verified on large, medium and small bridges.

2.3.3. Signal Processing Method (SPM)

Direct GNSS signal processing method (SPM) is another direct displacement detection method. [62].

The method is also based on the double-difference observations, and the displacement of the monitored point in the north, east, and upper directions between adjacent epochs can be calculated. The main formula is as follows:

$$
\begin{aligned}
L_{n,t_i} = \quad & \left(\cos\left(el_k^j\right).\cos\left(A_k^j\right) - \cos\left(el_k^i\right).\cos\left(A_k^i\right)\right)_{t_i}.N_{k,t_i} \\
& + \left(\cos\left(el_k^j\right).\sin\left(A_k^j\right) - \cos\left(el_k^i\right).\sin\left(A_k^i\right)\right)_{t_i}.E_{k,t_i} \\
& + \left(\sin\left(el_k^j\right) - \sin\left(el_k^i\right)\right)_{t_i}.U_{k,t_i}
\end{aligned}
\tag{19}
$$

where $L_{n,t_i}(n = 1, 2)$ is the filtered carrier phase double difference observation of nth frequency at epoch t_i; el_k^i and el_k^j are the elevation angles from the rover station to satellites; A_k^j and A_k^i are the azimuths from the rover station to satellites; $(N_{k,t_i}, E_{k,t_i}, U_{k,t_i})$ is the epoch-wise topocentric coordinate; coordinate; to estimate this coordinate, at least three double difference observations are required. The implementation of SPM mainly includes the following steps:

(1) Compute the double difference carrier phase observation at time t_i.
(2) High-pass filtering of the double-difference carrier phase observation sequence to remove long-term trend:

$$
L_{n,t_i} = filtered\left(\lambda_n \Delta\nabla\phi_{nkl}^{ij}(t)\right)_{t_i}
\tag{20}
$$

where $\lambda_n \Delta\nabla\phi_{nij}^{kl}(t)$ is the double difference carrier phase observation between receivers *k*, *l* and satellites *i*, *j* at time *t*.

(3) Calculate the azimuth and elevation angle of the satellite relative to the receiver at time t to form an observation equation.
(4) Estimate $(N_{k,t_i}, E_{k,t_i}, U_{k,t_i})$ by the least squares method.

For detailed derivation, please refer to the reference [62].

To study the accuracy of high-frequency RTK, PPP, SPM for dynamic detection under multiple constellations and different baseline length, a series of experiments were conducted. The results show that the method can provide reliable and consistent displacements with PPP and RTK. Compared with the traditional method, this method loses absolute position information and therefore cannot be used for long-term deformation monitoring. However, this method is not sensitive to the length of the baseline between rover and reference stations.

2.3.4. The Comparison of the Three Displacement Measurement Methods for SHM

Compared with the traditional positioning method for building dynamic monitoring, the above-mentioned methods have the following advantages:

- Easy implementation.
- Low computational overhead.
- No need to consider multi-system system bias.
- No need to consider multi-system frequency offset.

The three methods mentioned above all use the non-positioning pattern for dynamic monitoring, but they are not identical in principle and application, and there are similarities and differences. The comparison of the three is shown in Table 5.

Table 5. The comparison of the three displacement measurement methods for SHM.

	VADASE	PRM	SPM
Need reference station	No	Yes	Yes
GNSS receiver type	Single frequency Multi-frequency Multi-GNSS	Single frequency Multi-frequency Multi-GNSS	Single frequency Multi-frequency Multi-GNSS
Receiver sampling frequency requirement	High-rate	High-rate	High-rate
observations	Carrier phase	Double-differenced phase	Double-differenced phase
Principle	Difference between epochs	Select the phase residuals of two special satellites	Difference between epochs
Number of satellites	At least four common satellites in consecutive epochs	Two satellites in two special directions	At least four common satellites in consecutive epochs
Denoising or detrending	Yes	Yes	Yes

2.4. Single Frequency

The ionospheric error of data obtained from a single-frequency receiver cannot be corrected like a dual-frequency receiver. Single-frequency GPS-RTK is affected by the ionospheric delay, but research on it has never stopped due to its low cost [36,83]. To reduce the influence of the ionospheric error on single-frequency receivers, many scholars have studied the use of GNSS networks to correct the ionospheric errors of single-frequency receivers [36,84,85].

In Jiang et al. [84], a precise positioning service of the single-frequency receiver was implemented based on a non-differential CORS network model. This service is based on the undifferenced network RTK (URTK) [86]. The double difference ambiguities among the reference stations in the network and the corresponding carrier phase residual can be obtained by using relative positioning. Then, the double difference ambiguity can be converted to the undifferenced ambiguity using the URTK model. The local ionospheric and tropospheric disturbance can be modeled for a single frequency receiver by using the undifferenced observation residuals of reference stations. The service model was verified in the CORS network in Shanxi Province and Hubei Province, China. The findings show

that once the ambiguity is fixed, a single-frequency user can quickly obtain the absolute position with centimeter-level precision.

More attention should be paid to the low-reliability problem of single frequency positioning [83]. The initialization of single-frequency GPS RTK takes a few minutes, depending on the observation environment and the number of visible satellites [87,88]. In Cosser et al. [87], a study was conducted to verify the feasibility of using single-frequency GPS-RTK for bridge deformation and vibration monitoring. The experiment was carried out at the Wilford Suspension Footbridge over the River Trent in Nottingham. Single- and dual-frequency rover receivers connected via a splitter to the same antenna were used for comparison. Multipath effects and cycle slips were removed by adaptive filtering. When the dual-frequency reference station was located close to the rover station, the single-frequency rover can get accurate results. However, when the reference station was farther away from the rover station—about 3.6 km—the integer ambiguity of the rover can only be determined after setting the initial coordinate. This study at least illustrates the possibility of single-frequency GPS-RTK in bridge dynamic monitoring. A summary of the relevant studies about single-frequency GNSS for SHM is provided in Table 6. The information of experimental scene, aim, measurement method, and verification scheme are presented.

Table 6. Applications based on single-frequency GNSS for SHM.

Aim	Experimental Scene	Verification Scheme	Measurement Method	Literature
Single frequency GPS deformation monitoring	A bridge deformation monitoring network with four stations and another more complicated network in the southwest of USA			Huang et al. [83]
Verify the feasibility of using single-frequency GPS-RTK for bridge deformation and vibration monitoring.	Zero baseline trials and field bridge trials	Dual frequency RTK	Single frequency RTK	Cosser et al. [87]
Real-time PPP method of single frequency receiver based on CORS network	CORS network in Shanxi Province and Hubei Province, China	Dual frequency positioning result calculated by using GAMIT		Jiang et al. [84]
Verify the feasibility of single-frequency PPP-RTK	GPS Network Perth in Australia	The high-grade dual-frequency positioning result	Single-frequency PPP-RTK	Odijk et al. [85]

2.5. Comparison of Different Technologies for Dynamic Monitoring

As a traditional surveying technology, RTK is widely applied to SHM. However, its measurement accuracy will decrease with the increasing distance between the rover station and the reference station, and this method may fail when the reference station and the rover station are both located in the deformation area. Network RTK technology will provide wider coverage, and research about its application in SHM is at the early stage. As another precision positioning technology, PPP is widely used in seismology. The reference station is not required, but precise ephemeris is a must. However, there is no unified method to obtain real-time precise ephemeris. The research and application of dynamic monitoring based on PPP usually adopt post-processing. In addition, PPP technology itself has the problem of long initialization time. Compared with dual-frequency receivers, the price of single-frequency receivers is much lower, which is the reason why the research on single-frequency receivers has never stopped. The direct displacement measurement methods cannot obtain coordinates of monitoring stations but can obtain displacement changes in monitoring stations. In addition, these methods are not affected by inter-system and inter-frequency biases in multi-constellation system integration. The comparison of different technologies for dynamic monitoring is summarized in Table 7.

The improvement of GNSS-based dynamic monitoring for SHM from multi-GNSS, hardware as well as integration with other sensors is introduced in the next section.

Table 7. Comparison of different dynamic monitoring technologies for SHM.

Method		Pos mea	Ref stat	Research status	Pros	Cons
RTK	RTK	✓	✓	Applications [25–27,47,48]	Mature technology	Limited coverage The problem that the reference station is also in the deformation area
	Network RTK			Early-stage research [43]	Wide coverage Reliable	Needs service providers
	Single frequency RTK			Research [83,87]	Low-cost	Needs ionospheric corrections from reference stations
PPP	PPP	✓	✗	Applications [56,66]	No reference station required	Real-time data stream is needed
	Single frequency PPP			Research [84,85]	Low-cost	Long initialization time
GNSS & Accelerometer		✓		Applications [32,45,89–93]	Robust Complementary advantages	Data processing is relatively complex
Displacement Measurement	VADASE	✗	✗	Applications [67–75,94]	The integration of multi-GNSS systems is easier	Absence of absolute position, drifts
	PRM		✓	Applications [77–82,95]		
	SPM		✓	Research [62]		

Pos mea: Position measurement; Ref stat: Reference station.

3. Improvement of GNSS-Based Dynamic Monitoring Technologies for SHM

With the development of multi-GNSSs, the increasing of receiver sampling rates and the integration of GNSSs with other sensors, the GNSS-based dynamic monitoring technologies for SHM have been improved.

3.1. Multiple Constellations

In recent years, with the rapid development of GNSSs, more satellites and signals are available for navigation and positioning. On January 10, 2019, at 16:45, in Wuhan University, the user's visible satellites from different constellations are shown in Figure 7. More importantly, advances in multi-GNSS systems will address or partially address some of the issues in GNSS-based dynamic monitoring, such as the impact of deficient satellite geometry on dynamic monitoring.

The geometry between the receiver and the satellites affects positioning accuracy. When natural or artificial obstacles block the signal, it is difficult to obtain the desired positioning result. To solve this problem in deformation monitoring, many scholars have studied the use of pseudolites technology to improve the geometry between the receiver and satellites. Pseudolite is a ground-based satellite signal transmitter that improves the availability of signals [33,96–99]. Compared with the pseudolite, multi-constellation can improve the geometry between the receiver and satellites without additional investment.

There are currently two multi-constellation GNSS relative positioning combination models: one is loosely combined model and the other is the tightly combined model [100]. The loose combination means that different GNSSs choose their own satellite as the pivot satellite and the double-difference observation equation cannot be formed across systems, while the tight combination means that different GNSSs choose a common pivot satellite and the double-difference observation equation can be formed across systems [100,101]. For tight combinations, even if only one satellite is available in a constellation, it will be fully utilized as long as the total number of available satellites meets the requirements. To utilize differential positioning of the same frequency between different constellations,

the inter-system bias (ISB) between different constellations and receivers of different types should be calibrated first. The inter-system bias is the difference between the delay in the receiver that the different GNSSs' signals experience [102,103].
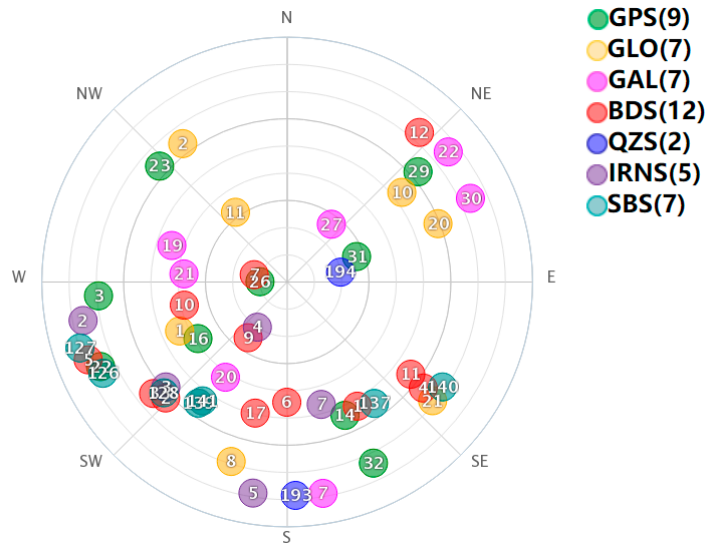

Figure 7. The skyplot of user's visible satellites from different constellations.

In Odijk et al. [103], to calibrate the ISB of overlapping frequencies from different GNSS constellations phase and code mixed observation models between GPS and Galileo were introduced. The differential ISBs between the GPS and Galileo of the receiver were calculated by a zero baseline calculation. The findings show that the differential ISB is only apparent between receivers of different types, and there is no differential ISB between the baselines of receivers of the same type. The results of the short baseline show that the calculated differential ISB can significantly improve the AR success rate of receivers of different types. In Odijk et al. [104], similarly, the receiver differential ISBs of the overlapping frequency between GPS and Galileo, Galileo and Beidou, as well as GPS and QZSS were calculated separately using a similar method.

The method mentioned above is used to calculate the ISB between GNSSs with overlapping frequencies. In Gao et al. [100], for different frequencies of different GNSS systems, to eliminate the differences between systems an inter-system difference model of different frequencies was proposed. Once the differential ISBs in the model are estimated, they can be used to enhance the system's availability in harsh environments. In the case of simulating the visibility of certain satellites, the collected data was processed using a traditional differential model and inter-system differential model, respectively. The results show that the inter-system difference model can significantly improve the positioning precision and reliability compared with the traditional difference model.

For PPP, the positioning technology is improved from the perspectives of initialization time and positioning accuracy. In Cai et al. [105], quad-constellation (GPS, BeiDou, GLONASS, Galileo) PPP model is proposed to simultaneously process the observations from all four GNSSs. The result shows that the quad-constellation PPP significantly improves the positioning accuracy and convergence time in comparison with the single-constellation and dual-constellations. In Li et al. [106], the accuracy and reliability of multi-GNSS (GPS, GLONASS, BeiDou, and Galileo) real-time precise positioning is investigated. The results show that the convergence time is reduced by 70% and the positioning accuracy is improved by 25% compared with the GPS-only method. In addition, as the cutoff elevation increases, the accuracy of multi-GNSS PPP is hardly decreased. Even as the cutoff height reaches 40 degrees, the accuracy of the horizontal component can still reach a few centimeters, which significantly improves its applicability in a constrained environment. In Geng et al. [107], a composite strategy is introduced to resolve GPS and GLONASS undifferenced ambiguities simultaneously to speed up initializations of

real-time PPP. The result shows that the average initializing time can be reduced from over 25 mins with GPS-only to about 6 mins with the GPS and GLONASS.

Similar to multi-GNSS RTK, there are many biases that should be taken into consideration in multi-GNSS PPP. By dealing with these biases, the convergence time of PPP is obviously reduced and the accuracy is slightly improved. Various types of biases in GNSS are reviewed, and the corresponding processing methods for these biases are proposed [108]. In Liu et al. [109], to assess PPP integer AR using GPS, GLONASS and BeiDou constellations, the fractional cycle bias (FCB) was estimated first. Then, the undifferenced PPP AR at each station was conducted to assess the contribution of using multi-GNSSs. The results show that the correct rate of AR increased significantly from 51.7% to 98.3%. A similar study was performed in Pan et al. [110]. In Geng et al. [111,112], a method was proposed to estimate station-specific phase biases (ISPBs). Then resolvable ambiguities between GNSSs (inter-system) instead of within GNSSs (intra-system) are formed for a more efficient partial AR. The average initialization time was reduced from 649 to 586 s. In addition, a preliminary theoretical framework to implement tightly coupled GNSS PPP model was provided.

Compared with single-constellation, multi-constellation means improved geometry between receiver and satellites and more available signals. Availability and reliability are improved, especially in harsh environments. Further research should be undertaken to explore multi-GNSS displacement measurement methods as well as integration with other sensors.

3.2. High-Rate GNSS Receiver

In SHM, the displacement, as well as the frequency of structures, are required to be measured [29]. SHM includes long-term deformation monitoring and short-term vibration detection. Experiments show that GNSS is not only suitable for long-term monitoring, but also for frequency measurement of structures, especially with the emergence of high-rate receivers.

3.2.1. Error Characteristics

To gain insight into high-rate GNSS receivers' error characteristics, many experiments were conducted [113–118].

In Moschasa et al. [114,119], static data from high-rate GNSS receivers of different types were collected to analyze the short-term measurement error characteristics of these receivers. The experiments were carried out in short baseline mode and the data was processed by using the Leica Geo Office (LGO) software in kinematic mode. Then the time series were decomposed into short- and long-period components by using a long-window high-pass moving average (running-average) filter for further analysis. The spectrum analysis shows that the low-frequency component, colored noise, will decay with the observation duration, and the high-frequency observation is mainly affected by white noise, which indicates that the high-frequency GNSS is suitable for structural dynamic monitoring.

On the other hand, the effects of GNSS receiver parameters on noise and correlation in high-rate measurements were studied [113,117]. In Moschas et al. [113], experiments with static GPS antennas and experiments with oscillating GPS antennas were conducted separately. In the above two sets of experiments, the phase-locked loop (PLL) bandwidth value of the GPS receivers of each set of experiments was set to 25, 50 and 100, respectively. By setting different PLL bandwidth values, the influence of this parameter on the correlation and noise of GNSS positioning results was studied. The results show that as the PLL bandwidth value increases, the noise of GNSS positioning results increases and the correlation decreases. For 100 Hz data collected using a pre-set PLL bandwidth equal to 100 Hz, the bandpass filtering method was used to filter out the noise to obtain the desired result, which is useful for monitoring high-frequency structural vibrations.

All of the studies mentioned above show that high-rate GNSS can be used to detect high-frequency components of structural vibrations [113,117].

3.2.2. Application

High-rate GNSS receivers essentially broaden the detection range of the frequency, which is of great significance for SHM. To study the applicability of high-rate GNSS for structural dynamic detection and seismology, a number of experiments were conducted.

To verify high-rate GNSS receivers for seismology, a series of controlled trials have been carried out [56,64,117]. In Moschas et al. [64], a series of free oscillation experiments were performed to assess the 10 Hz PPP for obtaining displacement waveforms. The experiments were based on an oscillator with a single degree of freedom (SDOF) carrying a GPS antenna and several other sensors, including an accelerometer. The oscillator was forced to a movement and then was left to oscillate until still. The assessment includes the sensitivity of high rate PPP for oscillations, the detection accuracy of the amplitude of oscillations, and the spectral coverage of the PPP record. The relative positioning was conducted for comparison using the TRACK software. The PPP processing was carried out using GIPSY-OASIS software and the online CSRS facility by the Natural Resources of Canada (CSRS), respectively. The results demonstrate that the waveforms of dynamic displacements can be reliably recorded, an overall accuracy about 5 mm can be achieved, and oscillations of frequency at least up to 4 Hz can be identified. In addition, many studies were conducted for seismology based on real high-rate GNSS data of earthquakes [65,72,90], which is of great sense for earthquake early warning. In Shi et al. [65], station displacements during the 12 May 2008 Mw 8.0 Wenchuan earthquake were derived from the 1 Hz GPS data collected during the earthquake. The data collected from the stations of the CORS network around the earthquake was processed by PNADA software in PPP mode. The data collected from the previous day was also processed to evaluate both the effect of multipath and other unmodeled errors, and the sidereal filter was applied in the position domain to mitigate the effect of the multipath. The results show that station oscillations caused by the earthquake of about 2 cm in amplitude can be detected reliably, and the estimated displacements are in agreement with the result obtained from the recently published rapture model.

Measurements of building vibration frequencies can be used to validate some computational models, such as the Finite Element (FE) model [29]. Therefore, the extraction of frequency information is important for the verification of building models. In addition, for a small bridge of 10 meters, its amplitude may reach several millimeters, and the vibration frequency may be 10 Hz [29,115], and traditional low-rate GNSS measurements cannot meet the requirements of many buildings with high modal frequencies. Various experiments were carried out to verify the high-rate GNSS for structure displacement detection [29,57,62,115]. In Roberts et al. [29], at the University of Nottingham, a series of experiments were conducted to demonstrate that high-rate receiver observations can be used for structural monitoring. In all experiments, the high-rate JNS100 receiver and the geodetic receiver Leica SR510 were connected to the same antenna via a splitter for comparison. Zero baseline experiments and short baseline experiments were carried out to assess the noise level of high-rate receivers under static observations. The results show that the high-rate JNS100 receiver measurement error is consistent with the geodetic receiver Leica SR510. To evaluate the two receivers' noise level in dynamic status, platform and bridge trials were carried out. The configuration of the bridge experiment was similar to the platform experiment, except for an accelerometer that was used for additional verification. The results show that the high-rate JNS100 measurement results are consistent with the Leica SR510 measurement results and the accelerometer integration results. In Yi et al. [115], similar work was carried out at the Dalian University of Technology, except for using the bridge FEM model as verification in field experiments. First, to study the noise characteristics of the receiver, a static experiment was performed. In this experiment, a short baseline consisting of two receivers were used for observation. The observation lasted for two days. The results show that the GNSS positioning noise contains many frequency components in the form of broadbands, and the main energy-intensive disturbances are distributed in the low-frequency region without an obvious periodic trend. Care must be taken when the frequency of the monitored building is in a low-frequency region of less than 1.5 Hz. To evaluate the dynamic measurement accuracy of high-rate GPS receivers, a dynamic evaluation experiment

was carried out. The results show that the high-rate GPS receiver can respond sensitively to dynamic vibrations. On-site assessment of the dynamic monitoring performance of high-rate GPS receivers was conducted at the Dalian BeiDa Bridge in China. To verify the high-frequency dynamic monitoring characteristics of the high-rate receiver, a series of data was collected on the bridge. The frequencies extracted from the high-frequency GPS receiver's measurement under ambient vibration excitation conditions are consistent with the frequencies calculated by the FEM, and one of the frequencies is greater than 10 Hz. The displacement value of the high-rate GPS receiver measurement is consistent with the calculated value of the FEM when a bus passes through the bridge. The same approach leads to the same conclusion when a fleet passes. All experiments have proved that high-rate GPS receivers can quantitatively describe bridge vibration, which is conducive to building verification and design. High-rate GPS receivers can be applied to measure high frequencies motions up to 10Hz and can provide 3D displacement information as well as frequency information of engineering structures, which is good for buildings' structural health and integrity monitoring.

A summary of the relevant studies mentioned above is provided in Table 8. The information of experimental scene, aim, sample rate, method, and verification scheme are presented.

Table 8. Applications based on high-rate receiver for SHM.

Aim	Sample Rate	Method	Experimental Scene	Verification Scheme	Literature
Noise characteristics of short-duration, GPS-records	10 Hz	Correlation analysis and spectral analysis of displacement time-series	Static observation		Moschasa et al. [114,119]
Noise characteristics and implications for monitoring networks	2–50 Hz	RTK			Genrich et al. [118]
PLL bandwidth and noise in GPS measurements	100 Hz	Correlation analysis and spectral analysis of displacement time-series			Moschas et al. [113]
Epoch-wise station displacement	1 Hz	PPP	GPS seismology	Rapture model	Shi et al. [65]
Broadband displacements	1 Hz	Loose integration		Acc	Bock et al. [90]
Evaluation of the variometric approach	1 Hz, 50 Hz	VADASE		PPP	Shu et al. [72]
Assessment of high-rate GPS for seismology	100 Hz	Correlation analysis of position	Shake table	ContT	Häberling et al. [117]
High-rate PPP for detecting dynamic vertical displacement	10 Hz	PPP	Bar experiment	ContT & RTK	Yigit et al. [57]
Precise dynamic displacements detection	50 Hz	PPP, RTK, SPM	Static observation		Paziewski et al. [62]
Measure seismic wave motions	10–50 Hz	PPP	GPS data and IMU data from shake table	IMU	Xu et al. [56]
Assessment of PPP accuracy for displacement waveforms	10 Hz	PPP	Experiment based on oscillator	Acc & DGPS	Moschas et al. [64]
Structural deflection monitoring	10 Hz, 50 Hz	RTK	Bridge	Acc	Roberts et al. [29]
Assessment of high-rate GPS receivers for deformation monitoring of bridges	50 Hz, 100 Hz	RTK	Bridge	Acc, FEM	Yi et al. [115]

Acc: Accelerometer, ContT: Controlled Test.

3.3. GNSSs & Accelerometers

As a traditional dynamic monitoring tool, accelerometers can be used to accurately identify high frequency vibrations in structures. More importantly, it is an independent system with less external

interferences [28,32]. Due to the high sampling frequency, the accelerometer is capable of extracting the acceleration response of a structure with a high natural frequency [33,120], so the accelerometer plays an important role in analyzing the structural response due to load conditions. Since the displacement through acceleration measurement is obtained indirectly through two integration processes, the error of displacement increases rapidly with time [93,121].

As a deformation monitoring technology, GNSSs can perform long-term and short-term monitoring of structures [32,90]. The real-time position of monitoring points can be obtained by GNSSs, and the displacement can be obtained by position difference. However, GNSS positioning precision is affected by factors such as the multipath effect, atmospheric error, observation noise, satellite geometry [121], etc., its sampling frequency is also limited, and the dynamic monitoring sensitivity is not as good as the accelerometer. Accelerometers and GNSSs have their own advantages and disadvantages. The combination of the two can make up for the deficiencies of a single system and greatly increase the reliability and productivity of the entire system by providing more measurements [32,121]. The integration of the two faces issues such as time synchronization and data fusion.

3.3.1. Time Synchronization

Accelerometers usually act as part of the IMU, so the time synchronization problem between GNSS and accelerometers is also the problem between GNSS and IMU. Time synchronization between IMU and the GNSS is the primary issue that needs to be addressed before data fusion [122–126].

In the early stages of GPS and accelerometer integration studies for deformation monitoring, the time synchronization problem between the accelerometer and GPS was solved by cross-correlation [32]. Cross-correlation is a common method for estimating the time delay between two signals [127,128]. The cross-correlation function is defined as follows:

$$R_{x_1 x_2}(\tau) = E[x_1(t) x_2(t - \tau)] \tag{21}$$

where E denotes the mathematical expectation operator; x_1 and x_2 are the two signals; τ is the time delay to be estimated. When $R_{x_1 x_2}$ reaches the maximum value, the corresponding τ is estimated as the time delay. This method was also used to check the consistency between the synchronization results of other methods and the reference [125].

However, the cross-correlation method cannot meet the requirements of real-time dynamic monitoring. The one pulse per second (1PPS) output of GPS receiver was introduced to solve the time synchronization problem of multi-sensor system. The main processing idea of this problem is to output a PPS from the GPS receiver as input to other sensors in the multi-sensor system as the reference time for others [124,125]. The main formula is as follows:

$$t_{imu}^{gps} = t_{pps}^{gps} + \left(t_{imu}^c - t_{pps}^c \right) \tag{22}$$

where t_{imu}^{gps} is the GPS time of IMU; t_{pps}^{gps} is the GPS time of the PPS; t_{imu}^c is the computer time of IMU; t_{pps}^c is the computer time of PPS; for more details, please refer to the references [123–126]. While the time between the consecutive PPS is one second, the actual alignment with the GPS second is unknown. There are offsets between different receivers' PPS [129]. The message from the receiver and counter are used to establish a link between the GPS time and the IMU time [124,125]. In applications where GNSSs and accelerometers are combined for deformation monitoring, many applications' synchronization schemes use the PPS output of an additional GNSS receiver as the reference time of the accelerometer to achieve time synchronization [44,45,93].

3.3.2. Integrated Design of the GNSS Antenna and Accelerometer

The lever arm effect is one of the main error sources for the GNSS/INS integrated navigation system. To suppress the lever arm effect between the GNSS antenna and the accelerometer in structural monitoring system, an integrated design of GNSS antenna and accelerometer was proposed [28].

The GNSS antenna and the accelerometer are connected to the base. The accelerometer is mounted on the device inside and below the cage. The disc is connected by three bolts in the middle. When the pedestal bubble is centered, the GNSS antenna, accelerometer, and pedestal center are coaxial, ensuring that multiple sensors monitor the same point, as shown in Figure 8.
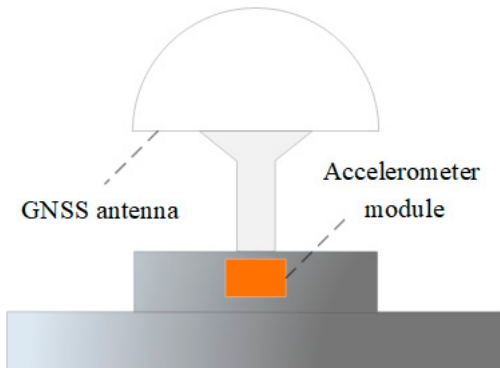

Figure 8. Integrated design of GNSS antenna and accelerometer for SHM [28].

3.3.3. Data Fusion

The data fusion methods of GNSS and accelerometer for dynamic monitoring can be classified into the isolated method and coupled method. Here, the isolated method refers to denoising, component extraction and checking using the correlation between the two signals. The coupled method is based on a rigorous mathematical derivation, the most representative of which is Kalman filtering.

Isolated Method

The displacement calculated from double integration of acceleration can be used to denoise the GPS positioning result. In Meng. [32], AF as already mentioned in Section 2.1.1 and will be detailed in Section 4.1, was introduced to deal with data fusion problems between accelerometers and GPS. The displacement calculated from the acceleration using the AF algorithm can be further used to mitigate receiver noise in GPS positioning results and detect true bridge movement. Due to the multipath error in the GPS positioning result, data fusion cannot be directly performed, so AF is applied to mitigate the multipath error. However, the detectable frequency range of the accelerometer assisted AF method cannot be widened and is limited to the detectable frequency range of the original GPS.

The absolute position can be achieved by GNSSs at each epoch, but the sampling rate is limited. The accelerometer has a high sampling frequency, but the calculated displacement is obtained by double integration, and is not suitable for low-frequency deformation monitoring. The combination of the two provides dynamic monitoring of structures with low and high frequencies [93,121]. In Chan et al. [93], to verify the accuracy and effectiveness of the combined algorithms using AF and empirical mode decomposition (EMD), a series of experiments based on a motion simulation table were performed. The types of vibrations in the experiment include white noise random waves, sinusoidal waves and wind-induced dynamic responses of the Di Wang building. The experimental results show that GPS is sensitive to multipath, and the monitoring of high frequency dynamic response is limited by the sampling rate. Accelerometers are not suitable for low frequency displacement monitoring. However, the combination of the two can handle these problems very well, and the overall displacement accuracy is significantly improved.

In addition, the acceleration data can be served as a check or constraint for the data process of GNSSs. In Moschas et al. [45], a short-span pedestrian bridge was monitored by GPS and acceleration, and the externally constrained multi-step filtering technology was adopted for data fusion to obtain the dynamic displacement and modal frequency of the bridge. Essentially, instead of merging GPS and accelerometer data, acceleration data acted as an external condition to constraint and evaluate

the entire process. The method consists of three steps. Firstly, the short-term components of the GPS measurements are calculated based on the supervised learning filter, and the accelerometer records are used for verification. Secondly, spectral analysis is performed on the first step results, the oscillation frequency is identified, and accelerometer data is used to evaluate the results of the spectral analysis. The frequency identified by this step will be used as the frequency of the next bandpass filter. Finally, the second filtering is performed, and the frequency range identified by the second step is used, and filtering is performed using a Chebyshev type filter to remove GPS observation noise. The test was carried out on a steel pedestrian footbridge crossing the Kifissos Avenue in Athens, Greece. During the test, a group of pedestrians jumped in the middle of the bridge to trigger the vibration. The results show that the method can detect the dynamic displacement of the order of >6 mm, and the estimated modal frequency is very consistent with the estimation results of accelerometer data.

Table 9 summarizes the above applications using GNSSs and accelerometers for dynamic monitoring. The information of experimental scene, fusion method, detail and limitations are presented.

Table 9. Applications using GNSS and accelerometer in isolated mode for SHM.

Experimental Scene	Fusion Method	Detail	Limitations	Literature
Bridge monitoring	AF	Acceleration aided the AF approach to isolate relative movements of the bridge	Detectable frequency is limited by the original GPS	Meng. [32]
Motion simulation table tests and super high-rise building monitoring data	Method based on AF and EMD	Enhanced the measurement of static and dynamic accuracy	Algorithm implementation is complicated	Chan et al. [93]
Dynamic displacement of steel pedestrian footbridge	A multi-step filtering procedure	Accelerometer was used to constrain and assess the filtering procedure	Accelerometer information is not fully utilized	Moschas et al. [45]

Kalman Filtering

Among the data fusion algorithm mentioned above, the accelerometer observations are either adopted as check values or as reference values for denoising GPS measurements. The drift caused by acceleration integration can be eliminated by means of mean removal or other detrending methods, but when permanent deformation occurs, erroneous results are obtained. In contrast to the isolated method, a multi-rate Kalman filter was proposed for data fusion of displacement and acceleration response measurements in dynamic monitoring, and the results show that the method can estimate the velocity and displacement more accurately even in the case of slowly changing and high observation noise [92,130]. The Kalman filter maintains real-time estimation of many parameters of the system, such as displacement and velocity, which may vary constantly, especially in dynamic monitoring scenarios. By utilizing the knowledge of deterministic and statistical characteristics of system parameters and measurements, Kalman filtering can obtain the best estimation with given available information. The random process and observation of discrete Kalman filter can be described as follows [131]:

$$x_{k+1} = \Phi_k x_k + w_k \tag{23}$$

$$z_k = H_k x_k + v_k \tag{24}$$

where x_k is the state vector; Φ_k is the transition matrix from t_k to t_{k+1}; z_k is the measurement vector; H_k is the observation matrix; w_k is Gaussian zero-mean white noise with covariance Q_k; v_k is the observation noise, and the corresponding covariance matric is R_k. The main steps of Kalman filtering are as follows:

The priori state estimate is calculated as follow

$$\hat{x}_k^- = \Phi_{k-1} \hat{x}_{k-1}^+ \tag{25}$$

The priori state covariance is updated as

$$P_k^- = \Phi_{k-1} P_{k-1}^+ \Phi_{k-1}^T + Q_{k-1} \qquad (26)$$

The Kalman gain can be obtained by

$$K_k = P_k^- H_k^T \left(H_k P_k^- H_k^T + R_k \right)^{-1} \qquad (27)$$

The posteriori state estimate and state covariance for error evaluation are calculated, respectively, as:

$$\hat{x}_k^+ = \hat{x}_k^- + K_k \left(z_k - H_k \hat{x}_k^- \right) \qquad (28)$$

$$P_k^+ = (I - K_k H_k) P_k^- \qquad (29)$$

The Kalman filter loop is given as Figure 9. For details of derivation, please refer to Brown et al. [132].

Enter prior estimate $\hat{x}_0^-$
and its error covariance P_0^-

Compute Kalman gain:
$$K_k = P_k^- H_k^T (H_k P_k^- H_k^T + R_k)^{-1}$$

$z_0, z_1, \cdots$

Prediction:
$$\hat{x}_k^- = \Phi_{k-1} \hat{x}_{k-1}^+$$
$$P_k^- = \Phi_{k-1} P_{k-1}^+ \Phi_{k-1}^T + Q_{k-1}$$

Update estimate with measurement:
$$\hat{x}_k^+ = \hat{x}_k^- + K_k (z_k - H_k \hat{x}_k^-)$$

$\hat{x}_0, \hat{x}_1, \cdots$

Error covariance of updated estimated:
$$P_k^+ = (I - K_k H_k) P_k^-$$
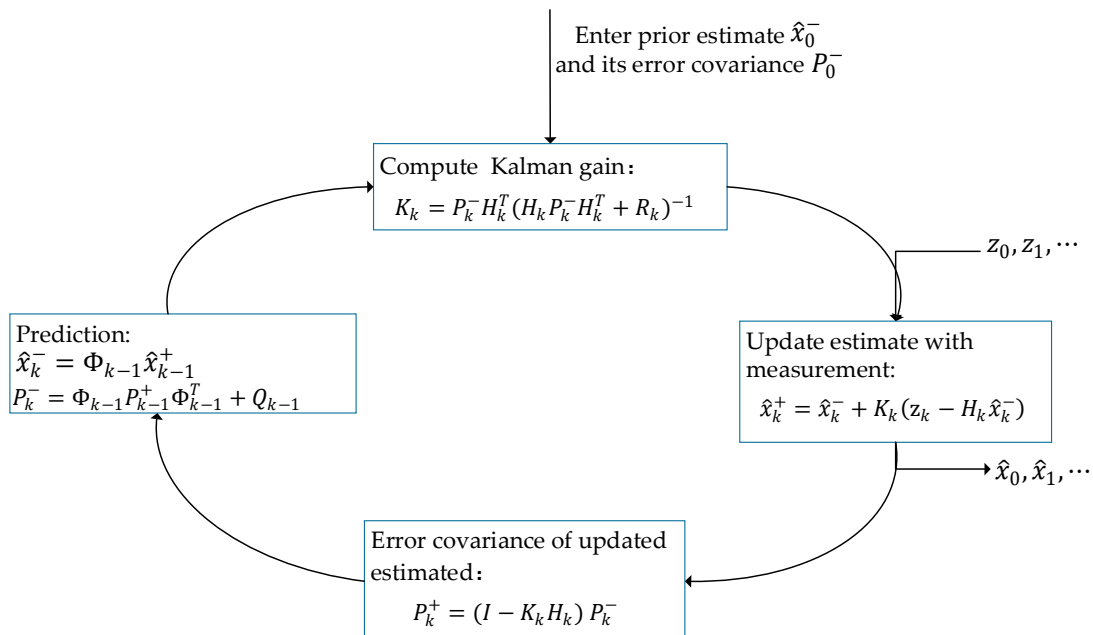
Figure 9. Kalman filter loop [132].

This technology has been widely applied to multi-sensor integration for dynamic monitoring [89–91,133–135]. According to the Nyquist theorem, the sensor's sampling rate must be at least two times of the vibration frequency of structures to detect the frequency of the vibration [72,136,137]. In Kogan et al. [91], the Kalman filter was applied to estimate the velocity and displacement of the load response on a large suspension bridge during the NYC marathon. The experiments were conducted by deploying 5 Hz GPS receivers and 100 Hz force-balance accelerometers (FBA) on the suspension bridge to extract load responses from human traffic. The Kalman filter was adopted to the data fusion of information from both sensors to obtain improved velocity and displacement estimation. Power spectrum analysis shows that a frequency component up to 2.7 Hz can be identified, which is higher than the Nyquist frequency of the GPS sampling. The results suggest that the method not only reduces the GPS observation noise but also expands the GPS detectable frequency range.

In seismology, Kalman filtering is a powerful tool for data fusion between GPS and strong accelerometer. In Bock et al. [90], this method was introduced to seismology to obtain more precise displacement. The method provides displacement of the accelerometer sampling rate with the precision of acceleration data and the accuracy of GPS data. Because of the respective characteristics of the GPS and accelerometer, the position accuracy provided by the GPS in each epoch is fixed, and the

displacement provided by the accelerometer is drifting, which are reflected in the Kalman filter process. Controllable test data and real seismic data were used to verify the accuracy improvement of ground displacement respectively. The shaking table test showed that the overall accuracy did not improve after the GPS sampling rate was increased to a certain value. The processing results of the 2010 El Mayor-Cucapah seismic data show that the Kalman filter can provide a significant increase in displacement accuracy and better characterize the seismic source.

Table 10 summarizes the above applications using Kalman filter for data fusion of GNSS and accelerometer. The information of experimental scene, aim, state variables and measurement are presented.

Table 10. Applications for SHM using Kalman filter for data fusion.

Aim	Experimental Scene	State Variables	Measurement	Literature
Multi-rate Kalman filtering for the data fusion	Simulation			Smyth et al. [92]
Providing a broadband record of ground displacements	Shake table experiments and earthquake data	Displacement and velocity	Displacement from GPS measurement	Bock et al. [90]
Load response on a large suspension bridge by GPS and accelerometers	A highway suspension bridge excited by marathon runners			Kogan et al. [91]
Low-cost RTK-GPS sensor and a force feedback accelerometer for infrastructure monitoring	Lab-scale vibration tests and field suspension bridge tests with a passing train	Displacement, velocity and acceleration	Displacement measurements from RTK-GPS	Koo et al. [89]

The data fusion between GNSS and accelerometers has undergone the following processes: initial isolation calculation, denoising, constraint assessment, and Kalman filtering for the loose combination. The overall development trend is from shallow to deep and will continue to move forward. In addition, the fusion mode between GNSS and other sensors needs further study.

4. Denoising and Detrending

The positioning accuracy of the GNSS is affected by factors such as the multipath effect, atmospheric error, observation noise, satellite geometry, etc. In addition, there are biases, scale factor error, and cross-coupling error as well as random noise in all kinds of accelerometers. Therefore, to identify the real vibration of structures, it is necessary to eliminate the trend and noise from the original observation. AF, Wavelet and EMD are the most widely used denoising and detrending methods in GNSS-based structure monitoring.

4.1. Adaptive Finite-Duration Impulse Response Filter (AF)

4.1.1. Theory

The algorithm starts with a set of predetermined initial conditions, representing whatever we know about the system. As a direct result of applying a recursive algorithm, where the parameters of the adaptive filter are updated from one adaptation cycle to the next, the parameters become dependent on the data. In a non-static environment, the algorithm provides tracking characteristics because as long as the change is slow enough, it tracks the temporal changes in the input data statistics, and the tracking results are ultimately reflected in the changes in the filtering parameters. Interference cancellation is one of the applications of AF. The AF is used to eliminate the unknown interference contained in the primary signal. The primary signal is used as the desired response of the adaptive filter and the reference signal is employed as the input to the filter. The reference signal is from a sensor or a set of sensors that provide a primary signal in a weak or substantially undetectable manner, wherein the information bearing signal component is weak. The adaptive filtering configuration for

noise cancellation is shown in Figure 10 below. where x is the input applied to the adaptive filter as the reference measurement, and the sequence form is expressed as x(n); y is the output of the adaptive filter, and the sequence form is expressed as y(n); d is the desired response as the primary measurement, and the sequence form is expressed as d(n); e is the estimation error, and the sequence form is expressed as e(n). The optimal parameter value of the FIR filter is selected by the adaptive algorithm with data from the estimation error. The FIR filter for estimating the output can be illustrated as [140]:

$$y(n) = \sum_{k=0}^{p} w_n(k)x(n-k) \tag{30}$$

where $w_n(k)$ is the coefficient or parameter of the Filter; the number of coefficients is p + 1.
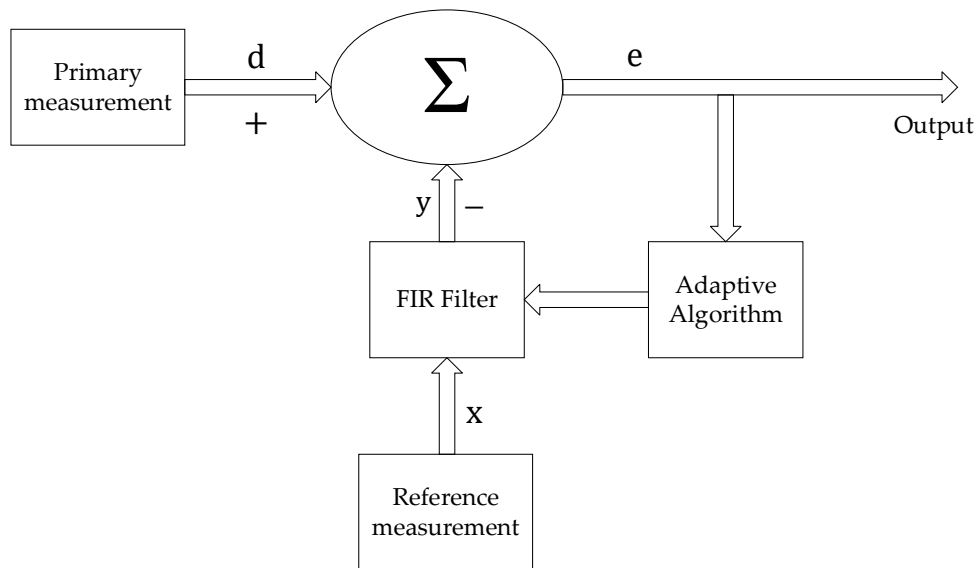
Figure 10. Adaptive filtering configuration, see Ge [138,139] for detail.

The error sequence e(n) can be formed by:

$$e(n) = d(n) - y(n) \tag{31}$$

x(n) and d(n) are assumed to be nonstationary random processes and the coefficients at time n are determined by minimizing the mean-square error:

$$\xi(n) = E(|e(n)|^2) \tag{32}$$

where E denotes the mathematical expectation operator. In practice, the coefficients of the Filter are selected by minimizing the sum of square error in a sample window as below:

$$\Psi = \sum_{n=0}^{M} |e(n)|^2 \ n = 0, \cdots, M \tag{33}$$

where M + 1 is the size of the sampling window. The gradient descent method is usually adopted to find the optimal coefficients, please refer to the reference for detail.

An example of AF for noise cancellation is demonstrated in Figure 11.
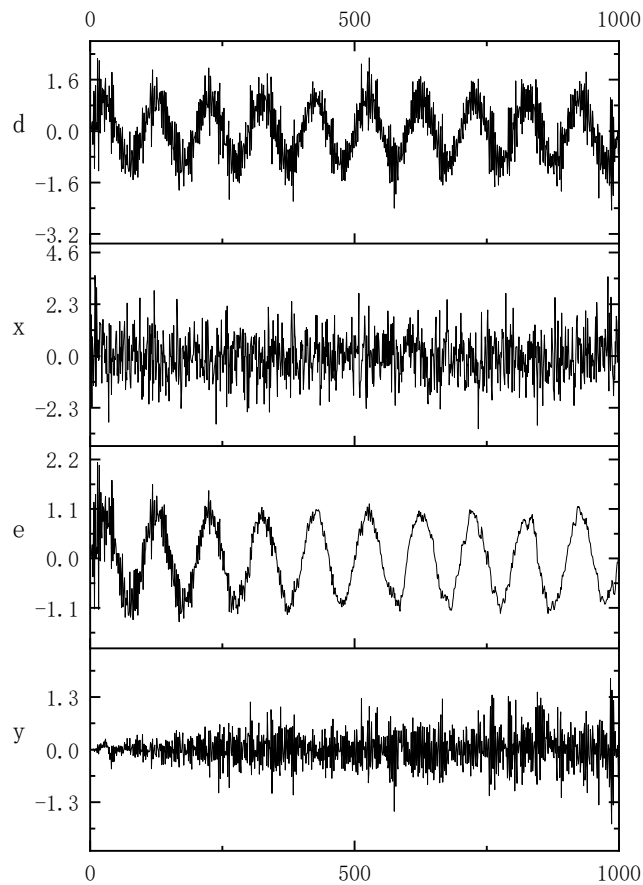
Figure 11. An example of AF.

4.1.2. Application

AF is a signal decomposer that uses the cross-correlation between the reference and the primary time series to extract the information of interest from the contaminated signal. Here, the applications of AF will be given from the perspective of the role of AF in the application. In Ge et al. [138,139], the AF method, based on a least-mean-square (LMS) algorithm, is used to mitigate multipath effects, and to derive fault movement signals from continuous GPS data. The method is applied to pseudo-range observation and carrier phase observation respectively for multipath mitigation. Forward filtering (previous day data as the reference time series) and backward filtering (previous day data as the primary time series) are tested separately. And the previous few days' data is tested respectively as primary signals. The results suggest that forward filtering using two consecutive days of data is the best filtering strategy. Application of AF in data fusion has been mentioned in Section 3.3.3.

In Chan et al. [93], the stationary GPS observation of the previous day is adopted as the reference to mitigating multipath and data from the accelerometer is taken as the reference to get low-frequency dynamic displacement.

In summary, the key to noise cancellation and component extraction using AF in GNSS-based SHM is how to select reference measurements. Since the structural dynamic monitoring scene is fixed, the multipath of GNSS has time repeatability, so the measured value of the previous stellar day can be adopted as a reference sequence to achieve the purpose of filtering out multipath [31–33,93,138,139]. Similarly, to obtain a low dynamic displacement response by the AF filter, the GPS measurement is adopted as the primary sequence, and the high-frequency dynamic displacement response of the accelerometer is adopted as the reference sequence [93].

4.2. Wavelet

4.2.1. Theory

Wavelet transform analysis has been developed for decades. Methods based on wavelet analysis have been widely used in signal denoising, outlier detection and bias separation and so on. The definition of continuous wavelet transform (CWT) is as follows [141]:

$$\text{CWT}(a, b) = \frac{1}{\sqrt{a}} \int_{-\infty}^{\infty} x(t) \psi\left(\frac{t-b}{a}\right) dt \tag{34}$$

where a is the scaling parameter; b is the time-shift parameter; $x(t)$ is the digital signal; ψ is a mother wavelet. Daughter wavelets can be obtained by scaling and shifting the mother wavelet. The time-shift parameter determines the location of the wavelet in the time domain while the scaling parameter determines the location of it in the frequency domain as well as the scale or extent of the time-frequency.

The scaling and shift parameter in CWT are real numbers that change continuously which are inconvenient for computation. The scaling and shift parameter are discretized, and the wavelet transformation can be described by two integers. The discrete wavelet transformation (DWT) is defined as [141]:

$$\text{DWT}(m, n) = \frac{1}{\sqrt{a_0^m}} \sum_k x[k] \psi\left[a_0^{-m} n - k\right] \tag{35}$$

where $x[k]$ is the signal; $\psi[\sim]$ is the mother wavelet; the integer m is the scaling parameter; the integer n is the time-shift parameter; a_0 is the scaling step.

Traditional spectrum analysis methods based on the Fourier transformation (FT) can only tell us what frequency components are contained in the signal. When these frequency components occur in the signal cannot be determined. However, the wavelet transform can obtain both time domain and frequency domain information. In particular, the wavelet transform is important for the analysis of dynamic monitoring, such as non-stationary GPS measurements. Wavelet analysis is an extension of the Fourier analysis and is more suitable for the analysis of dynamic changes [141,142]. The typical flow of wavelet analysis is shown in Figure 12 below.

```
┌─────────────────────┐
│      raw data       │
└─────────────────────┘
           ↓
┌─────────────────────┐
│ wavelet decomposition│
└─────────────────────┘
           ↓
┌─────────────────────┐
│     thresholding    │
└─────────────────────┘
           ↓
┌─────────────────────┐
│ wavelet reconstruction│
└─────────────────────┘
           ↓
┌─────────────────────┐
│    filtered data    │
└─────────────────────┘
```
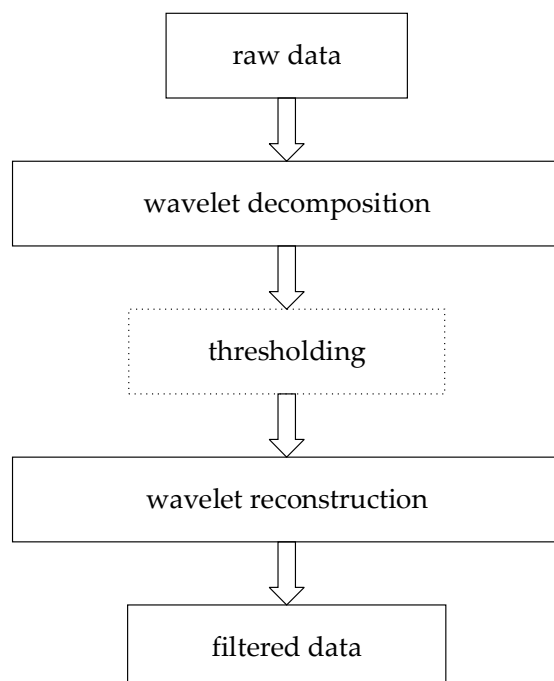
Figure 12. A typical block diagram of wavelet analysis [143].

As demonstrated in Figure 12, denoising using wavelet thresholding mainly includes the following steps [143,144]:

(1) Wavelet transformation:

Compute the wavelet transformation coefficients of the raw data: C_l, l is the index of coefficient, and the number of coefficients are determined by the mother wavelet.

(2) Denoising by thresholding

This step is done by comparing the magnitude of coefficient C_l with a threshold λ. The whole process is called thresholding. There are two commonly used thresholding: hard thresholding and soft thresholding.

Hard thresholding:

$$C_l^{(ht)} = \begin{cases} C_l, & if\ |C_l| > \lambda \\ 0, & otherwise \end{cases} \tag{36}$$

Soft thresholding:

$$C_l^{(st)} = \begin{cases} sign(C_l)(|C_l| - \lambda), & if\ |C_l| > \lambda \\ 0, & otherwise \end{cases} \tag{37}$$

(3) Inverse wavelet transforms

Perform the inverse wavelet transform by the denoised coefficients.
An example of wavelet denoising by thresholding is shown in Figure 13:
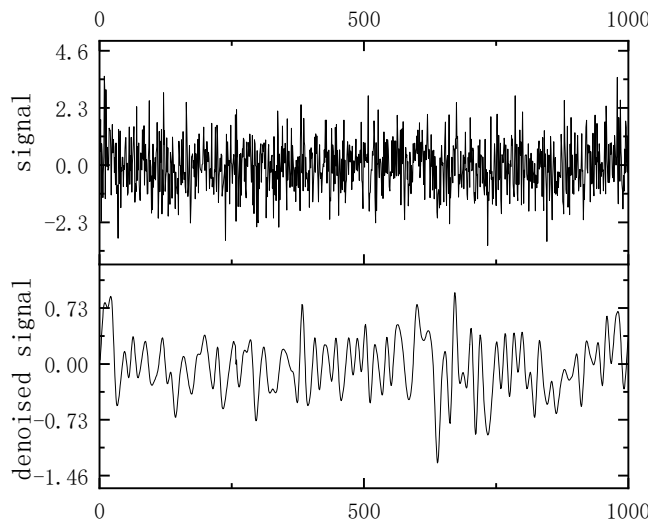
Figure 13. An example of wavelet denoising.

4.2.2. Application

Some applications of wavelets have been mentioned in Sections 2.1.3 and 2.3.2. More applications of wavelet will be given from the perspective of the role of wavelets in SHM.

Wavelet transformation is an effective technique for outlier(change) detection. On one hand, a signal can be decomposed into high- and low-frequency components by wavelet transformation for further processing. On the other hand, the power spectrum obtained by wavelet transformation can be used for intuitively identifying outliers. In Ogaja et al. [25], a wavelet analysis procedure is proposed to extract both the high and low frequencies of the structural dynamics from RTK-GPS results. First, the RTK-GPS results are decomposed into high-frequency components and low-frequency components by wavelet transformation. Then, the cumulative sum (CUSUM) algorithm [145,146] is applied to detect the change that has occurred in these components. The frequency change tests of high-to-high,

low-to-low, low-high are performed to validate this wavelet analysis procedure. In addition, the power spectrum with time and frequency information obtained by wavelet transformation can be directly used for change detection. In Kaloop et al. [46,147], DWT is tuned to detect abrupt changes in the response by decomposing the RTK-GPS result into approximate (low-frequency) and detailed (high-frequency) components, and the time–frequency map of the RTK-GPS results is generated by the CWT to analyze changes in structures' natural frequencies.

Also based on wavelet decomposition, the wavelet transform can also be used for bias separation. In Satirapod et al. [142], a new method of GPS data processing based on the wavelet decomposition is proposed. GPS double-differential residuals are decomposed into a low-frequency bias term and a high-frequency noise term based on wavelets, the extracted bias component is then applied directly to the GPS measurements for further processing. The final result of the method shows that the accuracy of the estimated baseline component is improved. Multipath error is generally considered to be a low-frequency component of GNSS positioning error, so a similar method was proposed for multipath mitigation [148].

In addition, wavelet transformation has been widely applied to denoising in GNSS positioning [144, 149–154]. In Wang et al. [150], an EMD and wavelet combined model is applied to extract the systematic errors from GPS double differential residual series. Selected high-frequency intrinsic mode functions (IMFs) are debossed by wavelet. The wavelet shrinkage noise reduction model based on soft-threshold was adopted to denoise the selected IMFS. Thereafter, the double differential carrier phase observations are modified by the extracted systematic errors epoch by epoch. The double differential observation equation is reconstructed and the float solution is calculated after that. The results show that the reliability and accuracy of the baseline solution are improved.

To sum up, the role of wavelets in GNSS-based SHM applications is divided into the following four categories: outlier (change) detection [25,46,143,147], bias separation [142], multipath mitigation [148], and denoising [144,149–154].

4.3. Empirical Mode Decomposition (EMD)

4.3.1. Theory

EMD is a signal processing method that can be used for nonlinear time series processing. This method is suitable for unmodeled system error handling [149,155–157]. Taking the multipath effect as an example, it is still a challenge to develop a general multipath correction model for different GNSS stations [158]. EMD decomposes the time series into a series of intrinsic mode functions (IMFs) and a residual. The whole process is an adaptive process, fully data-driven, without the need to define functions in advance. The main steps of EMD are as follows [159–165]:

(1) Find out the local maximum and minimum of the signal x(t), and the upper spline envelope $e_{up}(t)$ and the lower spline envelope $e_{low}(t)$ can be generated by using these extreme points, where t denotes time.

(2) Computing the means of upper and lower envelopes:

$$m_k(t) = \frac{e_{up}(t) + e_{low}(t)}{2}$$ (38)

where k denotes the loop index for calculating an IMF component.

(3) The difference between x(t) and $m_k(t)$ is calculated as:

$$d_k(t) = x(t) - m_k(t)$$ (39)

(4) $d_k(t)$ is verified to satisfy the conditions of IMF: (a) the number of extrema and the number of zero crossings are equal or at most differ by one in the entire signal; (b) $m_k(t)$ is zero for the entire signal. If these conditions are not met, $d_k(t)$ is adopted as the new 'x(t)' and the steps (1)–(4) are

repeated to calculate the nth IMF component. If these conditions are satisfied, $d_k(t)$ is adopted as the IMF component: $c_n(t)$, where n is the nth IMF component of original signal.

(5) The nth residual is calculated as:

$$r_n(t) = x(t) - \sum_{i=1}^{n} c_i(t) \tag{40}$$

(6) If the $r_n(t)$ is not monotonic, the $r_n(t)$ is adopted as the new '$x(t)$', and steps (1)–(6) are repeated to calculated the next IMF component. If the $r_n(t)$ is monotonic, the entire decomposition process is terminated, the original signal can be expressed as:

$$x(t) = \sum_{i=1}^{n} c_i(t) + r_n(t) \tag{41}$$

The EMD decomposition process is shown in Figure 14:
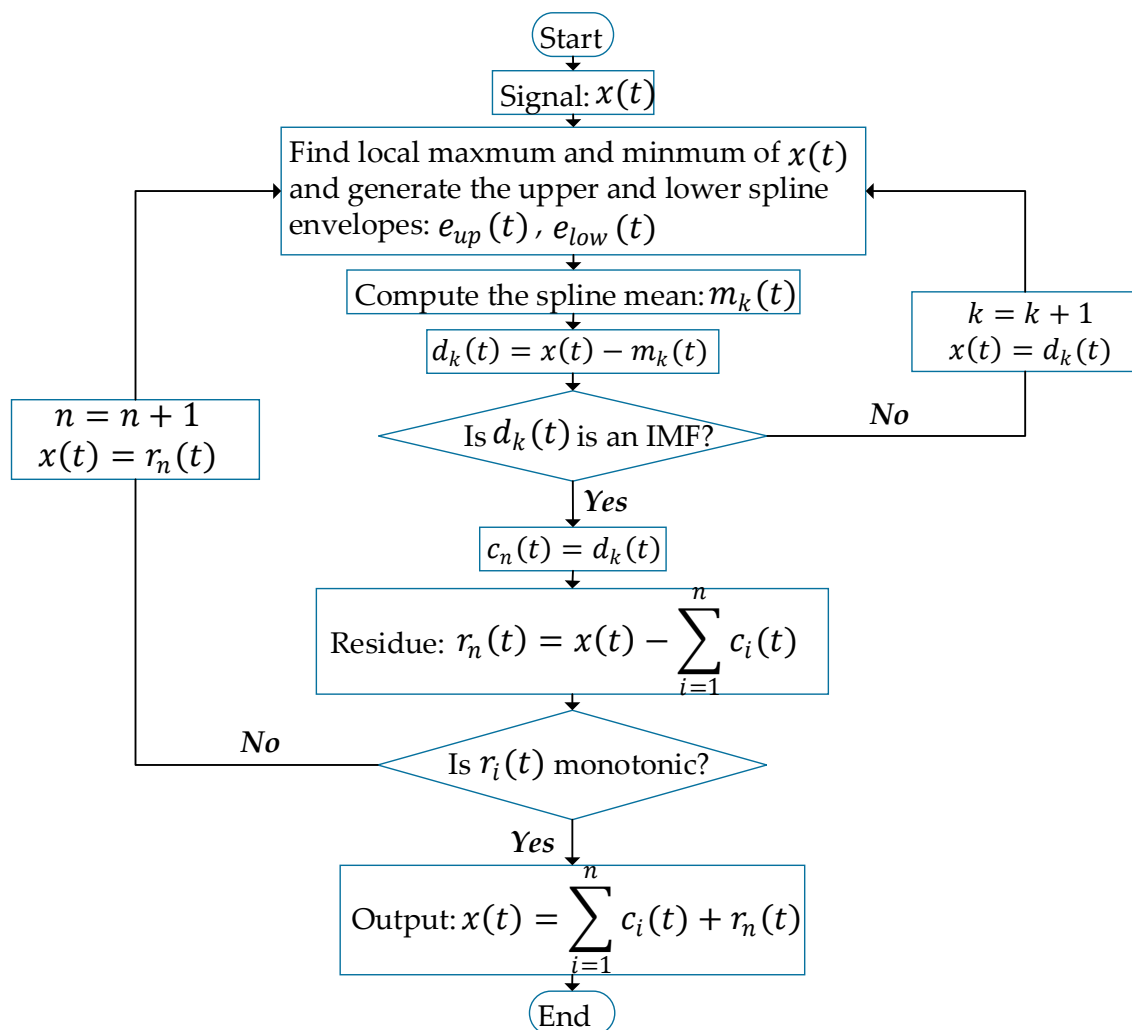
Figure 14. The flowchart of EMD [159–161].

An example of EMD decomposition is shown in Figure 15:
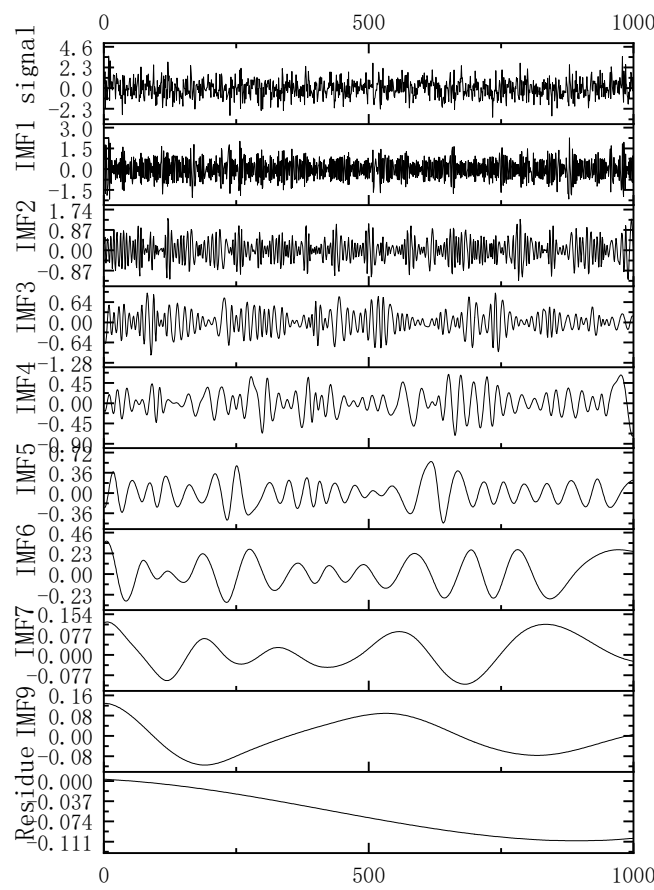
Figure 15. An example of EMD.

4.3.2. Application

Some of the GNSS-based SHM applications of EMD combined with other methods (AF, wavelet) are given in the Sections 3.3.3 and 4.3.2. Applications of GNSS-based SHM will be presented below, focusing on the role of EMD in data processing.

The existing body of research on EMD suggests that it is a powerful decomposition tool in time series analysis. Therefore, EMD is usually combined with other methods for data processing. In Chan et al. [93], an integrated GPS/accelerometer data processing technique based on empirical mode decomposition (EMD) and AF is proposed for SHM. The EMD is used to decompose the GPS measurement sequence and acceleration measurement sequence into a series of IMF components and final residuals, respectively. The high frequency IMF components (greater than a specified cutoff frequency) of the acceleration measurement sequence is adopted as the high-frequency dynamic displacement response. The residue component and the filtered IMF components (excluding the high frequency IMF components of acceleration measurement sequence by AF) of the GPS measurement sequence is adopted as the low-frequency dynamic displacement response. Motion simulation table tests were carried out to verify the processing technique. The results show that the overall displacement accuracy is significantly improved. In addition, many scholars also have studied the combination of EMD and wavelet transformation for data processing [149–151,157]. In Chao et al. [149], a combined model of EMD and wavelet is applied to extract the systematic errors from the residual series of double difference observation. EMD is used in data decomposition and reconstruction, while wavelet is employed for high-frequency signal denoising as mentioned in the previous section. The EMD-wavelet noise reduction model is shown in Figure 16. The extracted systematic errors are applied to the double difference observation as corrections. The recalculated results show that the method can effectively eliminate the unmodeled errors and improve the accuracy of the baseline solution.
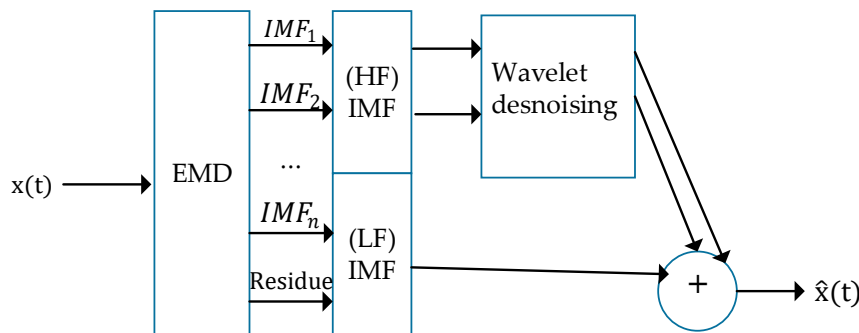
Figure 16. The flowchart of EMD-Wavelet trend extraction model [149].

There are also some other processing strategies based on EMD decomposition for different purposes [166–169]. In Chen et al. [166], the multipath effect is defined as the sum of residual and last a few IMF components. First, the GPS data of consecutive days is decomposed separately by EMD. Then, the correlation coefficient of the last a few IMFs in the consecutive days are calculated and the signal with maximum correlation coefficient value is the multipath effect. The proposed algorithm is validated using GPS measurements from controlled tests. The results show that the method can reliably mitigate the multipath effects in GPS data. In addition, EMD is used to extract white noise statistics in GPS coordinate time series. In Montillet et al. [169], an EMD-based algorithm is proposed to extract the white noise statistics in GPS coordinate time series. The first step in this algorithm is to decompose the GPS coordinate time series into sub-time sequences by EMD. After decomposition, the Hurst parameter of each sub-time sequence is estimated. Finally, the sub-time sequences in which Hurst parameter is less than 0.5 are selected to extract the white noise statistics. The algorithm is verified by the simulated coordinate time series and the actual coordinate time series respectively and the results show that the algorithm can greatly improve the computational efficiency with a slight increase in uncertainty compared to the maximum likelihood estimation.

Table 11 summarizes the applications using EMD for data decomposition of GNSS observation. The information of experimental scene, aim, and roles are presented.

Table 11. Applications using EMD for data decomposition.

Aim	Experimental Scene	Roles	Literature
GPS–accelerometer data integration for deformation monitoring	Motion simulation table tests	Decomposing the time history of GPS for final residuals. Decomposing the accelerator-measured dynamic displacement time history to extract high-frequency components.	Chan et al. [93]
Analysis and denoising of GPS Data	Simulation data and field GPS data	Denoising the white and colored noise	Baykut et al. [170]
Mine surveying of complex field conditions	field GPS/PLs data	Extracting the un-modeled systematic errors	Chao et al. [149]
Deformation monitoring based on the GPS/Pseudolites technology in open-pit mine	Simulation data and field GPS/PLs data		Jianpeng et al. [157]
Mining subsidence monitoring	Field GPS RTK		Chao et al. [155]
Reducing GPS carrier phase errors for precise static positioning	Field GPS data		Wang et al. [150]
GPS multipath effect Mitigation	A calibration test	Mitigating multipath effect	Chen et al. [166]
Multipath mitigation for GPS dynamic deformation monitoring	Simulation data and field GPS data		Dai et al. [167]
Assessing methods of RTK-GPS/accelerometer integration to monitor the displacement of structures	Field test data with reference from another sensor	Filtering of the acceleration data	Hwang et al. [168]
Extracting white noise statistics in GPS coordinate time series	Both simulated GPS coordinate time series and real data	Extracting White Noise Statistics	Montillet et al. [169]
Denoising GPS-based Structure monitoring data	Simulation data and field GPS data	Decomposing displacement for further processing	Ke. [151]

AF can be used for noise cancelation, but a reference measurement is required. Wavelet analysis can be used in signal denoising, outlier detection, and bias separation (detrending) and so on. EMD is suitable for unmodeled system error handling.

5. Conclusions

The purpose of this study was to review GNSS-based dynamic monitoring technologies for SHM. One of the more significant findings to emerge from this study is that GNSS-based dynamic monitoring technologies for SHM have been continuously developed with the development of GNSS. Presently, there are many GNSS constellations that can provide more satellites and signals, and high-precision monitoring results can be achieved even in harsh monitoring environments. The requirement for GNSS-based dynamic monitoring technology are more and more stringent, such as structure size from large to small, structure displacement from large to small, and structure modal frequency from low to high. High-rate receivers can provide a broader range of frequency detection, and studies have shown the feasibility of high-rate receivers for small buildings with small displacement amplitude and high vibration frequency. Cost is one of the factors that need to be considered for the wide-area implementation of SHM. The exploration of single-frequency monitoring technology aims to improve the detection precision to meet the monitoring requirements and thus reduce the hardware cost of SHM, while network RTK monitoring technology tries to reduce the cost of SHM in terms of greater coverage. Multi-sensor fusion for SHM is a trend in which each sensor complements its advantages, thereby improving overall monitoring reliability and precision. Some direct displacement measurement methods have been proposed for SHM. These displacement measurement methods have the advantages of small computational overhead, easy to implement, and no need to consider inter-system bias. Since GNSS observation is affected by factors, such as the multipath effect, atmospheric error, observation noise, and satellite geometry, denoising and detrending are indispensable, especially in complex SHM environments.

These findings have instructive implications for the study of low-cost, high-precision dynamic monitoring technologies for SHM and provide the following insights for future research:

i.   Currently, most receivers on the market support multi-GNSS and multi-frequencies. More research using controlled trials is needed to be done to evaluate the accuracy and reliability it can be achieved in its application for SHM.

ii.   Network RTK technology is an effective means to reduce the cost of large-scale SHM applications from the coverage perspective, and further research is needed to study the achievable monitoring accuracy within network coverage.

iii.   At present, the fusion of GNSS and other sensors for SHM is a loose combination, and the tight fusion between them needs further research. In addition, further research should be undertaken to investigate the cost and precision of multi-sensor fusion for SHM.

iv.   Currently, PPP-based dynamic monitoring for SHM is based on IGS precise ephemeris and clock products. The PPP-based dynamic monitoring for SHM based on real-time data stream service remains to be studied.

Author Contributions: Conceptualization, N.S. and L.C.; Methodology, N.S. and L.C.; Writing—original draft preparation, N.S.; Editing, L.C.; Review, J.L., L.W., T.T., R.C., and D.W.

Conflicts of Interest: The authors declare no conflict of interest.

References

1. Farrar, C.R.; Worden, K. An introduction to structural health monitoring. *Philos. Trans. R. Soc. A Math. Phys. Eng. Sci.* **2006**, *365*, 303–315. [CrossRef]

2. Sohn, H.; Farrar, C.R.; Hemez, F.M.; Shunk, D.D.; Stinemates, D.W.; Nadler, B.R.; Czarnecki, J.J. A review of structural health monitoring literature: 1996–2001. In Proceedings of the Third World Conference on Structural Control, Como, Italy, 7–12 April 2002.

3. Manzini, N.; Orcesi, A.; Thom, C.; Clément, A.; Botton, S.; Ortiz, M.; Dumoulin, J.; Mandé, F. Structural Health Monitoring using a GPS sensor network. In Proceedings of the 9th European Workshop on Structural Health Monitoring Series (EWSHM), Manchester, UK, 10–13 July 2018; p. 12.

4. Moss, R.; Matthews, S. In-service structural monitoring a state of the art review. *Struct. Eng.* **1995**, *73*, 23–31.

5. Mita, A.; Takhira, S. A smart sensor using a mechanical memory for structural health monitoring of a damage-controlled building. *Smart Mater. Struct.* **2003**, *12*, 204. [CrossRef]

6. Brownjohn, J.M. Structural health monitoring of civil infrastructure. *Philos. Trans. A Math. Phys. Eng. Sci.* **2007**, *365*, 589–622. [CrossRef] [PubMed]

7. Chang, F.-K. Structural Health Monitoring 2003: From Diagnostics & Prognostics to Structural Health Management. In Proceedings of the 4th International Workshop on Structural Health Monitoring, Stanford, CA, USA, 15–17 September 2003; DEStech Publications, Inc.: Lancaster, PA, USA, 2003; pp. 499–506.

8. Ogaja, C.; Li, X.; Rizos, C. Advances in structural monitoring with global positioning system technology: 1997–2006. *J. Appl. Geod. JAG* **2007**, *1*, 171–179. [CrossRef]

9. Yi, T.; Li, H.; Gu, M. Recent research and applications of GPS based technology for bridge health monitoring. *Sci. China Technol. Sci.* **2010**, *53*, 2597–2610. [CrossRef]

10. Yi, T.; Li, H.; Gu, M. Full-scale measurements of dynamic response of suspension bridge subjected to environmental loads using GPS technology. *Sci. China Technol. Sci.* **2010**, *53*, 469–479. [CrossRef]

11. Im, S.B.; Hurlebaus, S.; Kang, Y.J. Summary review of GPS technology for structural health monitoring. *J. Struct. Eng.* **2011**, *139*, 1653–1664. [CrossRef]

12. Rizos, C. Trends in GPS Technology & Applications. In Proceedings of the 2nd International LBS Workshop, Boston, MA, USA, 4 April 2009; Available online: http://citeseerx.ist.psu.edu/viewdoc/download?doi=10.1.1.640.3051&rep=rep1&type=pdf (accessed on 12 April 2019).

13. Dorides, C.D. *GNSS User Technology Report*; European GNSS Agency: Holešovice, Czechia, 2018; pp. 60–61. Available online: https://www.gsa.europa.eu/system/files/reports/gnss_user_tech_report_2018.pdf (accessed on 12 April 2019).

14. Wang, L.; Chen, R.; Li, D.; Zhang, G.; Shen, X.; Yu, B.; Wu, C.; Xie, S.; Zhang, P.; Li, M.; et al. Initial Assessment of the LEO Based Navigation signal augmentation System from Luojia-1A Satellite. *Sensors* **2018**, *18*, 3919. [CrossRef] [PubMed]

15. Bock, Y.; Prawirodirdjo, L.; Melbourne, T.I. Detection of arbitrarily large dynamic ground motions with a dense high-rate GPS network. *Geophys. Res. Lett.* **2004**, *31*, L06604.

16. Choi, K.; Bilich, A.; Larson, K.M.; Axelrad, P. Modified sidereal filtering: Implications for high-rate GPS positioning. *Geophys. Res. Lett.* **2004**, *31*. [CrossRef]

17. Hofmann-Wellenhof, B.; Lichtenegger, H.; Wasle, E. *GNSS–Global Navigation Satellite Systems: GPS, GLONASS, Galileo, and More*; Springer Science & Business Media: Berlin/Heidelberg, Germany, 2007; pp. 161–191.

18. Vollath, U.; Birnbach, S.; Landau, L.; Fraile-Ordoñez, J.M.; Martí-Neira, M. Analysis of Three-Carrier Ambiguity Resolution Technique for Precise Relative Positioning in GNSS-2. *Navigation* **1999**, *46*, 13–23. [CrossRef]

19. Leick, A.; Rapoport, L.; Tatarnikov, D. *GPS Satellite Surveying*; John Wiley & Sons: Hoboken, NJ, USA, 2015; pp. 257–357.

20. Teunissen, P.J. The least-squares ambiguity decorrelation adjustment: A method for fast GPS integer ambiguity estimation. *J. Geod.* **1995**, *70*, 65–82. [CrossRef]

21. Teunissen, P.; Joosten, P.; Tiberius, C. Geometry-free ambiguity success rates in case of partial fixing. In Proceedings of the 1999 National Technical Meeting of The Institute of Navigation, San Diego, CA, USA, 25–27 January 1999; pp. 201–207.

22. Teunissen, P.; Verhagen, S. GNSS carrier phase ambiguity resolution: Challenges and open problems. In *Observing Our Changing Earth*; Springer: Berlin/Heidelberg, Germany, 2009; pp. 785–792.

23. Wang, L.; Verhagen, S. A new ambiguity acceptance test threshold determination method with controllable failure rate. *J. Geod.* **2015**, *89*, 361–375. [CrossRef]

24. Wang, L.; Feng, Y.; Guo, J. Reliability control of single-epoch RTK ambiguity resolution. *GPS Solut.* **2016**, *21*, 591–604. [CrossRef]

25. Ogaja, C.; Rizos, C.; Wang, J.; Brownjohn, J. Toward the implementation of on-line structural monitoring using RTK-GPS and analysis of results using the wavelet transform. In Proceedings of the 10th FIG International Symposium on Deformation Measurements, Orange, CA, USA, 19–22 March 2001; pp. 19–22.

26. Ashkenazi, V.; Dodson, A.; Moore, T.; Roberts, G. Real time OTF GPS monitoring of the Humber Bridge. *Surv. World* **1996**, *4*, 26–28.

27. Ashkenazi, V.; Roberts, G. Experimental monitoring of the Humber Bridge using GPS. In *Institution of Civil Engineers-Civil Engineering*; Thomas Telford-ICE Virtual Library: London, UK, 1997; pp. 177–182.

28. Roberts, G.; Meng, X.; Dodson, A. The use of kinematic GPS and triaxial accelerometers to monitor the deflections of large bridges. In Proceedings of the 10th FIG International Symposium on Deformation Measurement, Orange, CA, USA, 19–22 March 2001; pp. 19–22.

29. Roberts, G.W.; Cosser, E.; Meng, X.; Dodson, A. High frequency deflection monitoring of bridges by GPS. *Positioning* **2004**, *1*, 226–231. [CrossRef]

30. Roberts, G.W.; Dodson, A.; Brown, C.; Karunar, R.; Evans, A. Monitoring the height deflections of the Humber Bridge by GPS, GLONASS, and finite element modelling. In *Geodesy Beyond 2000*; Springer: Berlin/Heidelberg, Germany, 2000; pp. 355–360.

31. Dodson, A.; Meng, X.; Roberts, G. Adaptive method for multipath mitigation and its applications for structural deflection monitoring. In Proceedings of the International Symposium on Kinematic Systems in Geodesy, Geomatics and Navigation (KIS 2001), Banff, AB, Canada, 5–8 June 2001; pp. 101–110.

32. Meng, X. Real-Time Deformation Monitoring of Bridges Using GPS/Accelerometers. Ph.D. Thesis, University of Nottingham, Nottingham, UK, 2002.

33. Meng, X.; Roberts, G.W.; Cosser, E.; Dodson, A.H.; Barnes, J.; Rizos, C. Real-time bridge deflection and vibration monitoring using an integrated GPS/accelerometer/pseudolite system. In Proceedings of the 11th International Symposium on Deformation Measurements, International Federation Surveyors (FIG), Commission 6-Engineering Surveys, Working Group, Santorini, Greece, 25–28 May 2003.

34. Meng, X.; Roberts, G.; Henry Roberts, A.; Dodson, S.; Ince, S.; Waugh, S. GNSS for structural deformation and deflection monitoring: Implementation and data analysis. In Proceedings of the 3rd IAG/12th FIG Symposium, Baden, Germany, 22–24 May 2006; pp. 22–24.

35. Vollath, U.; Landau, H.; Chen, X.; Doucet, K.; Pagels, C. Network RTK versus single base RTK–understanding the error characteristics. In Proceedings of the 15th International Technical Meeting of the Satellite Division of the Institute of Navigation, Portland, OR, USA, 24–27 September 2002; pp. 24–27.

36. Rizos, C. Network RTK research and implementation: A geodetic perspective. *J. Glob. Position. Syst.* **2002**, *1*, 144–150. [CrossRef]

37. Landau, H.; Vollath, U.; Chen, X. Virtual reference stations versus broadcast solutions in network RTK–advantages and limitations. In Proceedings of the GNSS 2003 European Navigation Conference, Graz, Austria, 22–25 April 2003.

38. Pepe, M. CORS architecture and evaluation of positioning by low-cost GNSS receiver. *Geod. Cartogr.* **2018**, *44*, 36–44. [CrossRef]

39. Stempfhuber, W. 3D-RTK capability of single GNSS receivers. *Int. Arch. Photogramm. Remote Sens. Spat. Inf. Sci.* **2013**, *40*, 379–384. [CrossRef]

40. Wübbena, G.; Bagge, A.; Schmitz, M. Network Based Techniques for RTK Applications. *GPS JIN* **2001**, 14–16.

41. Vollath, U.; Landau, H.; Chen, X. Network RTK–concept and performance. In Proceedings of the GNSS Symposium, Wuhan, China, 27–30 May 2002.

42. Vollath, U.; Buecherl, A.; Landau, H.; Pagels, C.; Wagner, B. Multi-base RTK positioning using virtual reference stations. In Proceedings of the ION GPS, Salt Lake City, UT, USA, 19–22 September 2000; pp. 123–131.

43. Yu, J.; Yan, B.; Meng, X.; Shao, X.; Ye, H. Measurement of bridge dynamic responses using network-based real-time kinematic GNSS technique. *J. Surv. Eng.* **2016**, *142*, 04015013. [CrossRef]

44. Yu, J.; Meng, X.; Shao, X.; Yan, B.; Yang, L. Identification of dynamic displacements and modal frequencies of a medium-span suspension bridge using multimode GNSS processing. *Eng. Struct.* **2014**, *81*, 432–443. [CrossRef]

45. Moschas, F.; Stiros, S. Measurement of the dynamic displacements and of the modal frequencies of a short-span pedestrian bridge using GPS and an accelerometer. *Eng. Struct.* **2011**, *33*, 10–17. [CrossRef]

46. Kaloop, M.; Hu, J.; Elbeltagi, E. Adjustment and Assessment of the Measurements of Low and High Sampling Frequencies of GPS Real-Time Monitoring of Structural Movement. *ISPRS Int. J. Geo-Inf.* **2016**, *5*, 222. [CrossRef]

47. Kaloop, M.R.; Hu, J.W. Dynamic Performance Analysis of the Towers of a Long-Span Bridge Based on GPS Monitoring Technique. *J. Sens.* **2016**, *2016*, 7494817. [CrossRef]

48. Elnabwy, M.T.; Kaloop, M.R.; Elbeltagi, E. Talkha steel highway bridge monitoring and movement identification using RTK-GPS technique. *Measurement* **2013**, *46*, 4282–4292. [CrossRef]

49. Bisnath, S.; Gao, Y. Precise point positioning. *GPS World* **2009**, *20*, 43–50.

50. Bisnath, S.; Gao, Y. Current state of precise point positioning and future prospects and limitations. In *Observing Our Changing Earth*; Springer: Berlin/Heidelberg, Germany, 2009; pp. 615–623.

51. Zumberge, J.; Heflin, M.; Jefferson, D.; Watkins, M.; Webb, F. Precise point positioning for the efficient and robust analysis of GPS data from large networks. *J. Geophys. Res. Solid Earth* **1997**, *102*, 5005–5017. [CrossRef]

52. Kouba, J.; Héroux, P. Precise point positioning using IGS orbit and clock products. *GPS Solut.* **2001**, *5*, 12–28. [CrossRef]

53. Teunissen, P.; Khodabandeh, A. Review and principles of PPP-RTK methods. *J. Geod.* **2015**, *89*, 217–240. [CrossRef]

54. Shen, X. Improving Ambiguity Convergence in Carrier Phase-Based Precise Point Positioning. Ph.D. Thesis, Department of Geomatics Engineering, University of Calgary, Calgary, AB, Canada, 2002.

55. Witchayangkoon, B. Elements of GPS Precise Point Positioning. Ph.D. Thesis, Spatial Information Science and Engineering, University of Maine, Orono, ME, USA, 2000.

56. Xu, P.; Shi, C.; Fang, R.; Liu, J.; Niu, X.; Zhang, Q.; Yanagidani, T. High-rate precise point positioning (PPP) to measure seismic wave motions: An experimental comparison of GPS PPP with inertial measurement units. *J. Geod.* **2013**, *87*, 361–372. [CrossRef]

57. Yigit, C.O.; Gurlek, E. Experimental testing of high-rate GNSS precise point positioning (PPP) method for detecting dynamic vertical displacement response of engineering structures. *Geomat. Nat. Hazards Risk* **2017**, *8*, 893–904. [CrossRef]

58. Xu, C.-H.; Wang, J.-L.; Gao, J.-X.; Jian, W.; Hong, H. Precise point positioning and its application in mining deformation monitoring. *Trans. Nonferrous Met. Soc. China* **2011**, *21*, s499–s505. [CrossRef]

59. Hu, H.; Gao, J.; Yao, Y. Land deformation monitoring in mining area with PPP-AR. *Int. J. Min. Sci. Technol.* **2014**, *24*, 207–212. [CrossRef]

60. Martín, A.; Anquela, A.B.; Dimas-Pagés, A.; Cos-Gayón, F. Validation of performance of real-time kinematic PPP. A possible tool for deformation monitoring. *Measurement* **2015**, *69*, 95–108. [CrossRef]

61. Song, W.; Zhang, R.; Yao, Y.; Liu, Y.; Hu, Y. PPP Sliding Window Algorithm and Its Application in Deformation Monitoring. *Sci. Rep.* **2016**, *6*, 26497. [CrossRef] [PubMed]

62. Paziewski, J.; Sieradzki, R.; Baryla, R. Multi-GNSS high-rate RTK, PPP and novel direct phase observation processing method: Application to precise dynamic displacement detection. *Meas. Sci. Technol.* **2018**, *29*, 035002. [CrossRef]

63. Yigit, C.O. Experimental assessment of post-processed kinematic Precise Point Positioning method for structural health monitoring. *Geomat. Nat. Hazards Risk* **2016**, *7*, 360–383. [CrossRef]

64. Moschas, F.; Avallone, A.; Saltogianni, V.; Stiros, S.C. Strong motion displacement waveforms using 10-Hz precise point positioning GPS: An assessment based on free oscillation experiments. *Earthq. Eng. Struct. Dyn.* **2014**, *43*, 1853–1866. [CrossRef]

65. Shi, C.; Lou, Y.-D.; Zhang, H.-P.; Zhao, Q.; Geng, J.; Wang, R.; Fang, R.; Liu, J. Seismic deformation of the Mw 8.0 Wenchuan earthquake from high-rate GPS observations. *Adv. Space Res.* **2010**, *46*, 228–235. [CrossRef]

66. Kaloop, M.R.; Rabah, M. Time and frequency domains response analyses of April 2015 Greece's earthquake in the Nile Delta based on GNSS-PPP. *Arab. J. Geosci.* **2016**, *9*, 316. [CrossRef]

67. Colosimo, G.; Crespi, M.; Mazzoni, A. Real-time GPS seismology with a stand-alone receiver: A preliminary feasibility demonstration. *J. Geophys. Res. Solid Earth* **2011**, *116*, B11302. [CrossRef]

68. Benedetti, E.; Branzanti, M.; Biagi, L.; Colosimo, G.; Mazzoni, A.; Crespi, M. Global Navigation Satellite Systems seismology for the 2012 M w 6.1 Emilia earthquake: Exploiting the VADASE algorithm. *Seismol. Res. Lett.* **2014**, *85*, 649–656. [CrossRef]

69. Branzanti, M.; Colosimo, G.; Crespi, M.; Mazzoni, A. GPS near-real-time coseismic displacements for the great Tohoku-oki earthquake. *IEEE Geosci. Remote Sens. Lett.* **2013**, *10*, 372–376. [CrossRef]

70. Hung, H.-K.; Rau, R.-J.; Benedetti, E.; Branzanti, M.; Mazzoni, A.; Colosimo, G.; Crespi, M. GPS Seismology for a moderate magnitude earthquake: Lessons learned from the analysis of the 31 October 2013 ML 6.4 Ruisui (Taiwan) earthquake. *Ann. Geophys.* **2017**, *60*, 0553. [CrossRef]

71. Geng, T.; Xie, X.; Fang, R.; Su, X.; Zhao, Q.; Liu, G.; Li, H.; Shi, C.; Liu, J. Real-time capture of seismic waves using high-rate multi-GNSS observations: Application to the 2015 Mw 7.8 Nepal earthquake. *Geophys. Res. Lett.* **2016**, *43*, 161–167. [CrossRef]

72. Shu, Y.; Fang, R.; Li, M.; Shi, C.; Li, M.; Liu, J. Very high-rate GPS for measuring dynamic seismic displacements without aliasing: Performance evaluation of the variometric approach. *GPS Solut.* **2018**, *22*, 121. [CrossRef]

73. Fratarcangeli, F.; Savastano, G.; D'Achille, M.; Mazzoni, A.; Crespi, M.; Riguzzi, F.; Devoti, R.; Pietrantonio, G. VADASE reliability and accuracy of real-time displacement estimation: Application to the Central Italy 2016 earthquakes. *Remote Sens.* **2018**, *10*, 1201. [CrossRef]

74. Ashcroft, N.; Youssef, T.; Anthony, C. Leica VADASE: First Autonomous GNSS Monitoring Solution. Available online: http://www.fig.net/resources/proceedings/fig_proceedings/fig2016/papers/ts07b/TS07B_ashcroft_tawk_et_al_7952.pdf (accessed on 12 April 2019).

75. Savastano, G.; Fratarcangeli, F.; Chiara D'Achille, M.; Mazzoni, A.; Crespi, M. Recent advances of VADASE to enhance reliability and accuracy of real-time displacements estimation. In Proceedings of the EGU General Assembly Conference Abstracts, Vienna, Austria, 23–28 April 2017; p. 11486.

76. Benedetti, E.; Ravanelli, R.; Moroni, M.; Nascetti, A.; Crespi, M. Exploiting Performance of Different Low-Cost Sensors for Small Amplitude Oscillatory Motion Monitoring: Preliminary Comparisons in View of Possible Integration. *J. Sens.* **2016**, *2016*, 7490870. [CrossRef]

77. Schaal, R.E.; Larocca, A.P.C. A Methodology for Monitoring Vertical Dynamic Sub-Centimeter Displacments with GPS. *GPS Solut.* **2002**, *5*, 15–18. [CrossRef]

78. Larocca, A.P.C.; Schaal, R.E.; Guimarães, G. d. N.; da Silveira, I.M.; Segantine, P.C.L. Frequency Structures Vibration Identified by an Adaptative Filtering Techiques Applied on GPS L1 Signal. *Positioning* **2013**, *4*, 137. [CrossRef]

79. Larocca, A.P.C. Using high-rate GPS data to monitor the dynamic behavior of a cable-stayed bridge. In Proceedings of the 17th International Technical Meeting of the Satellite Division of the US Institute of Navigation, Long Beach, CA, USA, 21–24 September 2004.

80. Larocca, A.P.C.; Schaal, R.E.; Santos, M.; Langley, R. Monitoring the deflection of the Pierre-Laporte suspension bridge with the phase residual method. In Proceedings of the 18th International Technical Meeting of the Satellite Division of The Institute of Navigation, Long Beach, CA, USA, 13–16 September 2005; pp. 2023–2028.

81. Larocca, A.P.C.; de Araújo Neto, J.O.; Trabanco, J.L.A.; dos Santos, M.C.; Barbosa, A.C.B. First Steps Using Two GPS Satellites for Monitoring the Dynamic Behavior of a Small Concrete Highway Bridge. *J. Surv. Eng.* **2016**, *142*, 04016008. [CrossRef]

82. Larocca, A.P.C.; Neto, J.; Barbosa, A.; Trabanco, J.L.A.; Da Cunha, A.L.B.N. Dynamic Monitoring vertical Deflectionof Small Concrete Bridge Using Conventional Sensors And 100 Hz GPS Receivers—Preliminary Results. *IOSR J. Eng.* **2014**, *4*, 9–20. [CrossRef]

83. Huang, S.; Wang, J. New data processing strategy for single frequency GPS deformation monitoring. *Surv. Rev.* **2015**, *47*, 379–385. [CrossRef]

84. Jiang, W.; Zou, X.; Tang, W. A New Kind of Real-Time PPP Method for GPS Single-Frequency Receiver Using CORS Network. *Chin. J. Geophys.* **2012**, *55*, 284–293. [CrossRef]

85. Odijk, D.; Teunissen, P.J.; Zhang, B. Single-frequency integer ambiguity resolution enabled GPS precise point positioning. *J. Surv. Eng.* **2012**, *138*, 193–202. [CrossRef]

86. Zou, X.; Ge, M.; Tang, W.; Shi, C.; Liu, J. URTK: Undifferenced network RTK positioning. *GPS Solut.* **2013**, *17*, 283–293. [CrossRef]

87. Cosser, E.; Roberts, G.W.; Meng, X.; Dodson, A.H. The comparison of single frequency and dual frequency GPS for bridge deflection and vibration monitoring. In Proceedings of the Deformation Measurements and Analysis, 11th International Symposium on Deformation Measurements, International Federation of Surveyors (FIG), Commission 6-Engineering Surveys, Working Group 6.1, Santorini, Greece, 25–28 May 2003.

88. He, H.; Li, J.; Yang, Y.; Xu, J.; Guo, H.; Wang, A. Performance assessment of single-and dual-frequency BeiDou/GPS single-epoch kinematic positioning. *GPS Solut.* **2014**, *18*, 393–403. [CrossRef]

89. Koo, G.; Kim, K.; Chung, J.Y.; Choi, J.; Kwon, N.Y.; Kang, D.Y.; Sohn, H. Development of a High Precision Displacement Measurement System by Fusing a Low Cost RTK-GPS Sensor and a Force Feedback Accelerometer for Infrastructure Monitoring. *Sensors* **2017**, *17*, 2745. [CrossRef] [PubMed]

90. Bock, Y.; Melgar, D.; Crowell, B.W. Real-time strong-motion broadband displacements from collocated GPS and accelerometers. *Bull. Seismol. Soc. Am.* **2011**, *101*, 2904–2925. [CrossRef]

91. Kogan, M.G.; Kim, W.-Y.; Bock, Y.; Smyth, A.W. Load response on a large suspension bridge during the NYC Marathon revealed by GPS and accelerometers. *Seismol. Res. Lett.* **2008**, *79*, 12–19. [CrossRef]

92. Smyth, A.; Wu, M. Multi-rate Kalman filtering for the data fusion of displacement and acceleration response measurements in dynamic system monitoring. *Mech. Syst. Signal Process.* **2007**, *21*, 706–723. [CrossRef]

93. Chan, W.; Xu, Y.; Ding, X.; Dai, W. An integrated GPS–accelerometer data processing technique for structural deformation monitoring. *J. Geod.* **2006**, *80*, 705–719. [CrossRef]

94. Benedetti, E.; Branzanti, M.; Colosimo, G.; Mazzoni, A.; Crespi, M. VADASE: State of the Art and New Developments of a Third Way to GNSS Seismology. In Proceedings of the VIII Hotine-Marussi Symposium on Mathematical Geodesy, Rome, Italy, 17–21 June 2013; Springer: Berlin/Heidelberg, Germany, 2015; pp. 59–66.

95. Schaal, R.E.; Larocca, A.P.C.; Guimarães, G.N. Use of a single L1 GPS receiver for monitoring structures: First results of the detection of millimetric dynamic oscillations. *J. Surv. Eng.* **2011**, *138*, 92–95. [CrossRef]

96. Dai, L.; Wang, J.; Tsujii, T.; Rizos, C. Inverted pseudolite positioning and some applications. *Surv. Rev.* **2002**, *36*, 602–611. [CrossRef]

97. Dai, L.; Zhang, J.; Rizos, C.; Han, S.; Wang, J. GPS and pseudolite integration for deformation monitoring applications. In Proceedings of the 13th International Technical Meeting of the Satellite Division of the US Institute of Navigation (ION-GPS 2000), Salt Lake City, UT, USA, 19–22 September 2000; pp. 1–8.

98. Rizos, C. *Pseudolite augmentation of GPS*; School of Surveying & Spatial Information Systems, University of New South Wales: Sydney, Australia, 2005; Available online: http://citeseerx.ist.psu.edu/viewdoc/download?doi=10.1.1.66.3605&rep=rep1&type=pdf (accessed on 2 April 2019).

99. Cellmer, S.; Rapinski, J.; Rzepeca, Z. Pseudolites and their Applications. In Proceedings of the INGEO 2011—5th International Conference on Engineering Surveying, Brijuni, Croatia, 22–24 September 2011; pp. 269–278.

100. Gao, W.; Meng, X.; Gao, C.; Pan, S.; Wang, D. Combined GPS and BDS for single-frequency continuous RTK positioning through real-time estimation of differential inter-system biases. *GPS Solut.* **2018**, *22*, 20. [CrossRef]

101. Julien, O.; Alves, P.; Cannon, M.E.; Zhang, W. A tightly coupled GPS/GALILEO combination for improved ambiguity resolution. In Proceedings of the European Navigation Conference (ENC-GNSS'03), Calgary, AB, Canada, 9 September 2003; pp. 1–14.

102. Hegarty, C.; Powers, E.; Fonville, B. Accounting for timing biases between GPS, modernized GPS, and Galileo signals. In Proceedings of the 36th Annual Precise Time and Time Interval Systems and Applications Meeting, Washington, DC, USA, 7–9 December 2004; pp. 307–318.

103. Odijk, D.; Teunissen, P. Characterization of Between-Receiver GPS-Galileo Inter-System Biases and their Effect on Mixed Ambiguity Resolution. *GPS Solut.* **2013**, *17*, 521–533. [CrossRef]

104. Odijk, D.; Teunissen, P.J. Estimation of differential inter-system biases between the overlapping frequencies of GPS, Galileo, BeiDou and QZSS. In Proceedings of the 4th International Colloquium Scientific and Fundamental Aspects of the Galileo Programme, Prague, Czech Republic, 4–6 December 2013; pp. 4–6.

105. Cai, C.; Gao, Y.; Pan, L.; Zhu, J. Precise point positioning with quad-constellations: GPS, BeiDou, GLONASS and Galileo. *Adv. Space Res.* **2015**, *56*, 133–143. [CrossRef]

106. Li, X.; Ge, M.; Dai, X.; Ren, X.; Fritsche, M.; Wickert, J.; Schuh, H. Accuracy and reliability of multi-GNSS real-time precise positioning: GPS, GLONASS, BeiDou, and Galileo. *J. Geod.* **2015**, *89*, 607–635. [CrossRef]

107. Geng, J.; Shi, C. Rapid initialization of real-time PPP by resolving undifferenced GPS and GLONASS ambiguities simultaneously. *J. Geod.* **2017**, *91*, 361–374. [CrossRef]

108. El-Mowafy, A.; Deo, M.; Rizos, C. On biases in precise point positioning with multi-constellation and multi-frequency GNSS data. *Meas. Sci. Technol.* **2016**, *27*, 035102. [CrossRef]

109. Liu, Y.; Lou, Y.; Ye, S.; Zhang, R.; Song, W.; Zhang, X.; Li, Q. Assessment of PPP integer ambiguity resolution using GPS, GLONASS and BeiDou (IGSO, MEO) constellations. *GPS Solut.* **2017**, *21*, 1647–1659. [CrossRef]

110. Pan, L.; Xiaohong, Z.; Fei, G. Ambiguity resolved precise point positioning with GPS and BeiDou. *J. Geod.* **2017**, *91*, 25–40. [CrossRef]

111. Geng, J.; Guo, J.; Chang, H.; Li, X. Toward global instantaneous decimeter-level positioning using tightly coupled multi-constellation and multi-frequency GNSS. *J. Geod.* **2018**, 1–15. [CrossRef]

112. Geng, J.; Li, X.; Zhao, Q.; Li, G. Inter-system PPP ambiguity resolution between GPS and BeiDou for rapid initialization. *J. Geod.* **2019**, *93*, 383–398. [CrossRef]

113. Moschas, F.; Stiros, S. PLL bandwidth and noise in 100 Hz GPS measurements. *GPS Solut.* **2015**, *19*, 173–185. [CrossRef]

114. Moschasa, F.; Stiros, S. Noise characteristics of short-duration, high frequency GPS-records. *Adv. Math. Comput. Tools Metrol. Test.* **2012**, *9*, 1488–1506.

115. Yi, T.-H.; Li, H.-N.; Gu, M. Experimental assessment of high-rate GPS receivers for deformation monitoring of bridge. *Measurement* **2013**, *46*, 420–432. [CrossRef]

116. Niu, X.; Chen, Q.; Zhang, Q.; Zhang, H.; Niu, J.; Chen, K.; Shi, C.; Liu, J. Using Allan variance to analyze the error characteristics of GNSS positioning. *GPS Solut.* **2014**, *18*, 231–242. [CrossRef]

117. Häberling, S.; Rothacher, M.; Zhang, Y.; Clinton, J.; Geiger, A. Assessment of high-rate GPS using a single-axis shake table. *J. Geod.* **2015**, *89*, 697–709. [CrossRef]

118. Genrich, J.F.; Bock, Y. Instantaneous geodetic positioning with 10–50 Hz GPS measurements: Noise characteristics and implications for monitoring networks. *J. Geophys. Res. Solid Earth* **2006**, *111*. [CrossRef]

119. Moschas, F.; Stiros, S. Noise characteristics of high-frequency, short-duration GPS records from analysis of identical, collocated instruments. *Measurement* **2013**, *46*, 1488–1506. [CrossRef]

120. Roberts, G.W.; Meng, X.; Dodson, A.H. Integrating a global positioning system and accelerometers to monitor the deflection of bridges. *J. Surv. Eng.* **2004**, *130*, 65–72. [CrossRef]

121. Li, X.; Rizos, C.; Ge, L.; Tamura, Y.; Yoshida, A. The complementary characteristics of GPS and accelerometer in monitoring structural deformation. In Proceedings of the ION 2005 Meeting, Long Beach, CA, USA, 13–16 September 2005.

122. Knight, D.T. Achieving modularity with tightly-coupled GPS/INS. In Proceedings of the PLANS'92 Position Location and Navigation Symposium Record, Monterey, CA, USA, 23–27 March 1992; pp. 426–432.

123. Li, B. A cost effective synchronization system for multisensor integration. In Proceedings of the ION GNSS, Long Beach, CA, USA, 21–24 September 2004; pp. 1627–1635.

124. Li, B.; Rizos, C.; Lee, H.K.; Lee, H.K. A GPS-slaved time synchronization system for hybrid navigation. *GPS Solut.* **2006**, *10*, 207–217. [CrossRef]

125. Ding, W.; Wang, J.; Li, Y.; Mumford, P.; Rizos, C. Time synchronization error and calibration in integrated GPS/INS systems. *ETRI J.* **2008**, *30*, 59–67. [CrossRef]

126. Ding, W.; Wang, J.; Mumford, P.; Li, Y.; Rizos, C. Time synchronization design for integrated positioning and georeferencing systems. In Proceedings of the SSC 2005 Spatial Intelligence, Innovation and Praxis: The National Biennial Conference of the Spatial Sciences Institute, Melbourne, Australia, 12–16 September 2005; pp. 1265–1274.

127. Knapp, C.; Carter, G. The generalized correlation method for estimation of time delay. *IEEE Trans. Acoust. Speechand Signal Process.* **1976**, *24*, 320–327. [CrossRef]

128. Ianniello, J. Time delay estimation via cross-correlation in the presence of large estimation errors. *IEEE Trans. Acoust. Speechand Signal Process.* **1982**, *30*, 998–1003. [CrossRef]

129. Mumford, P. Timing characteristics of the 1PPS output pulse of three GPS receivers. In Proceedings of the 6th International Symposium on Satellite Navigation Technology Including Mobile Positioning & Location Services, Melbourne, Australia, 22–25 July 2003; p. 45.

130. Smyth, A.; Wu, M.; Kogan, M. Data fusion of GPS displacements and acceleration response measurements for large scale bridges. In Proceedings of the 4th World Conference on Structural Control and Monitoring, San Diego, CA, USA, 11–13 July 2006; p. 13.

131. Grewal, M.S.; Andrews, A.P. *Kalman Filtering: Theory and Practice Using MATLAB*; John Wiley & Sons, Inc.: Hoboken, NJ, USA, 2008; pp. 138–172.

132. Brown, R.G.; Hwang, P.Y. *Introduction to Random Signals and Applied Kalman Filtering: With MATLAB Exercises*; John Wiley & Sons, Inc.: Hoboken, NJ, USA, 2012; pp. 141–172.

133. Kim, J.; Kim, K.; Sohn, H. Autonomous dynamic displacement estimation from data fusion of acceleration and intermittent displacement measurements. *Mech. Syst. Signal Process.* **2014**, *42*, 194–205. [CrossRef]

134. Kim, K.; Choi, J.; Koo, G.; Sohn, H. Dynamic displacement estimation by fusing biased high-sampling rate acceleration and low-sampling rate displacement measurements using two-stage Kalman estimator. *Smart Struct. Syst.* **2016**, *17*, 647–667. [CrossRef]

135. Kim, K.; Sohn, H. Dynamic displacement estimation by fusing LDV and LiDAR measurements via smoothing based Kalman filtering. *Mech. Syst. Signal Process.* **2017**, *82*, 339–355. [CrossRef]

136. Nyquist, H. Certain topics in telegraph transmission theory. *Trans. Am. Inst. Electr. Eng.* **1928**, *47*, 617–644. [CrossRef]

137. Smalley, R., Jr. High-rate gps: How High do we need to go? *Seismol. Res. Lett.* **2009**, *80*, 1054–1061. [CrossRef]

138. Ge, L.; Chen, H.-Y.; Han, S.; Rizos, C. Adaptive filtering of continuous GPS results. *J. Geod.* **2000**, *74*, 572–580. [CrossRef]

139. Ge, L.; Han, S.; Rizos, C. Multipath mitigation of continuous GPS measurements using an adaptive filter. *GPS Solut.* **2000**, *4*, 19–30. [CrossRef]

140. Haykin, S.O. *Adaptive Filter Theory*; Pearson Higher Ed: London, UK, 2013; pp. 19–47.

141. El-Shimy, N.; Osman, A.; Nassar, S.; Noureldin, A. Wavelet Multiresolution Analysis. *GPS World* **2003**, *60*. [CrossRef]

142. Satirapod, C.; Ogaja, C.; Wang, J.; Rizos, C. GPS analysis with the aid of wavelets. In Proceedings of the International Symposium Satellite Navigation Technology & Applications, Canberra, Australia, 24–27 July 2001.

143. Aram, M.; El-Rabbany, A.; Krishnan, S.; Anpalagan, A. Single frequency multipath mitigation based on wavelet analysis. *J. Navig.* **2007**, *60*, 281–290. [CrossRef]

144. Lau, L. Wavelet packets based denoising method for measurement domain repeat-time multipath filtering in GPS static high-precision positioning. *GPS Solut.* **2017**, *21*, 461–474. [CrossRef]

145. Mertikas, S.; Rizos, C. On-line detection of abrupt changes in the carrier-phase measurements of GPS. *J. Geod.* **1997**, *71*, 469–482. [CrossRef]

146. Mertikas, S.P. Automatic and online detection of small but persistent shifts in GPS station coordinates by statistical process control. *GPS Solut.* **2001**, *5*, 39–50. [CrossRef]

147. Kaloop, M.R.; Li, H. Sensitivity and analysis GPS signals based bridge damage using GPS observations and wavelet transform. *Measurement* **2011**, *44*, 927–937. [CrossRef]

148. Azarbad, M.R.; Mosavi, M. A new method to mitigate multipath error in single-frequency GPS receiver with wavelet transform. *GPS Solut.* **2014**, *18*, 189–198. [CrossRef]

149. Chao, L.; Feng, Z.; Yan, L. GPS/Pseudolites technology based on EMD-wavelet in the complex field conditions of mine. *Procedia Earth Planet. Sci.* **2009**, *1*, 1293–1300. [CrossRef]

150. Wang, J.; Wang, J.; Roberts, C. Reducing GPS carrier phase errors with EMD-wavelet for precise static positioning. *Surv. Rev.* **2009**, *41*, 152–161. [CrossRef]

151. Ke, L. Denoising GPS-Based Structure Monitoring Data Using Hybrid EMD and Wavelet Packet. *Math. Probl. Eng.* **2017**, *2017*, 4920809. [CrossRef]

152. Yuan, D.; Cui, X.; Wang, G.; Jin, J.; Fan, D.; Jia, X. Study on the GPS Data De-noising Method Based on Wavelet Analysis. In Proceedings of the International Conference on Computer and Computing Technologies in Agriculture, Beijing, China, 29–31 October 2011; Springer: Berlin/Heidelberg, Germany, 2011; pp. 390–399.

153. Kaloop, M.R.; Kim, D. De-noising of GPS structural monitoring observation error using wavelet analysis. *Geomat. Nat. Hazards Risk* **2016**, *7*, 804–825. [CrossRef]

154. Hussan, M.; Kaloop, M.R.; Sharmin, F.; Kim, D. GPS Performance Assessment of Cable-Stayed Bridge using Wavelet Transform and Monte-Carlo Techniques. *KSCE J. Civ. Eng.* **2018**, *22*, 4385–4398. [CrossRef]

155. Liu, C.; Zhou, F.; Gao, J.; Wang, J. Some problems of GPS RTK technique application to mining subsidence monitoring. *Int. J. Min. Sci. Technol.* **2012**, *22*, 223–228. [CrossRef]

156. Li, Y.; Xu, C.; Yi, L.; Fang, R. A data-driven approach for denoising GNSS position time series. *J. Geod.* **2018**, *92*, 905–922. [CrossRef]

157. Jianpeng, W.; Jingxiang, G.; Chao, L.; Jian, W. High precision slope deformation monitoring model based on the GPS/Pseudolites technology in open-pit mine. *Min. Sci. Technol. (China)* **2010**, *20*, 126–132.

158. Wang, M.; Wang, J.; Dong, D.; Li, H.; Han, L.; Chen, W. Comparison of Three Methods for Estimating GPS Multipath Repeat Time. *Remote Sens.* **2018**, *10*, 6. [CrossRef]

159. Gairola, G.S.; Chandrasekhar, E. Heterogeneity analysis of geophysical well-log data using Hilbert–Huang transform. *Phys. A Stat. Mech. Its Appl.* **2017**, *478*, 131–142. [CrossRef]

160. Bin Queyam, A.; Kumar Pahuja, S.; Singh, D. Quantification of feto-maternal heart rate from abdominal ECG signal using empirical mode decomposition for heart rate variability analysis. *Technologies* **2017**, *5*, 68. [CrossRef]

161. Bagherzadeh, A.; Sabzehparvar, M. A local and online sifting process for the empirical mode decomposition and its application in aircraft damage detection. *Mech. Syst. Signal Process.* **2015**, *54*, 68–83. [CrossRef]

162. Rosero, J.; Romeral, L.; Ortega, J.; Urresty, J. Demagnetization fault detection by means of Hilbert Huang transform of the stator current decomposition in PMSM. In Proceedings of the 2008 IEEE International Symposium on Industrial Electronics, Cambridge, UK, 30 June–2 July 2008; pp. 172–177.

163. Huang, N.E.; Shen, Z.; Long, S.R.; Wu, M.C.; Shih, H.H.; Zheng, Q.; Yen, N.-C.; Tung, C.C.; Liu, H.H. The empirical mode decomposition and the Hilbert spectrum for nonlinear and non-stationary time series analysis. *Proc. R. Soc.* **1998**, *454*, 903–995. [CrossRef]

164. Xu, Y.; Chen, J. Characterizing nonstationary wind speed using empirical mode decomposition. *J. Struct. Eng.* **2004**, *130*, 912–920. [CrossRef]

165. Chen, J.; Xu, Y. On modelling of typhoon-induced non-stationary wind speed for tall buildings. *Struct. Des. Tall Spec. Build.* **2004**, *13*, 145–163. [CrossRef]

166. Chen, J.; Shang, X.; Zhao, X. GPS multipath effect mitigation algorithm based on empirical mode decomposition. In Proceedings of the 12th Biennial International Conference on Engineering, Construction, and Operations in Challenging Environments; and Fourth NASA/ARO/ASCE Workshop on Granular Materials in Lunar and Martian Exploration, Honolulu, HI, USA, 14–17 March 2010.

167. Dai, W.; Huang, D.; Cai, C. Multipath mitigation via component analysis methods for GPS dynamic deformation monitoring. *GPS Solut.* **2014**, *18*, 417–428. [CrossRef]

168. Hwang, J.; Yun, H.; Park, S.-K.; Lee, D.; Hong, S. Optimal methods of RTK-GPS/accelerometer integration to monitor the displacement of structures. *Sensors* **2012**, *12*, 1014–1034. [CrossRef]

169. Montillet, J.-P.; Tregoning, P.; McClusky, S.; Yu, K. Extracting white noise statistics in GPS coordinate time series. *IEEE Geosci. Remote Sens. Lett.* **2013**, *10*, 563–567. [CrossRef]

170. Baykut, S.; Akgul, T.; Ergintav, S. EMD-based analysis and denoising of GPS data. In Proceedings of the IEEE 17th Signal Processing and Communications Applications Conference, Antalya, Turkey, 9–11 April 2009; pp. 644–647.